Synthesis of Nanomaterials and their Composites for Energy Conversion and Storage

IISER PUNE

Thesis Submitted towards the Partial fulfillment of BS-MS dual degree programme

By

UPENDRA SINGH

Under the Guidance of

Prof. SATISHCHANDRA B OGALE

Chief Scientist

Physical and Materials Chemistry Department

National Chemical Laboratory

Pune

To

The Department of Chemistry

INDIAN INSTITUTE OF SCIENCE EDUCATION AND RESEARCH

PUNE

Dedicated to my beloved parents and teachers...

CERTIFICATE

This is to certify that this dissertation entitled **"Synthesis of Nanomaterials and their Composites for Energy Conversion and Storage"** is towards the partial fulfilment of the BS-MS dual degree programme at the Indian Institute of Science Education and Research Pune and represents original research carried out by **Upendra Singh** at Physical and Materials Chemistry Department, National Chemical Laboratory, Pune under the Supervision of **Prof. Satishchandra B. Ogale** during the academic year 2013-2014.

Prof. S.B. Ogale

(Supervisor)

Date: 02, April 2014

Place: **Pune**

Dr. Partha Hazra

(Local Coordinator)

Date: 02, April 2014

Place: **Pune**

Prof. K.N. Ganesh

(H.O.D of Chemistry)

Date: 02, April 2014

Place: **Pune**

<u>DECLARATION</u>

I hereby declare that the matter embodied in the thesis entitled **"Synthesis of Nanomaterials and their Composites for Energy Conversion and Storage"** are the results of the investigations carried out by me at the Department of Physical and Materials Chemistry, National Chemical Laboratory (NCL) Pune, under the supervision of Prof. Satishchandra B Ogale and the same has not been submitted elsewhere for any other degree.

Place: Pune   **UPENDRA SINGH**

02, April 2014   **Reg No. 20091018**

ACKNOWLEDGEMENT

CONTENTS

List of Abbreviations

0D	Zero Dimensional
1D	One Dimensional
2D	Two Dimensional
3D	Three Dimensional
BET	Brunauer Emmett Teller
C_s	Specific Capacitance
CNT	Carbon Nanotube
CV	Cyclic Voltammetry
CVD	Chemical Vapor Deposition
CCG	Chemically Converted Graphene
D.I.	De Ionized
ED	Electron Diffraction
EDL	Electric Double Layer
EDLC	Electrochemical Double Layer Capacitor
EIS	Electrochemical Impedance Spectroscopy
ESR	Equivalent Series Resistance
EV	Electric Vehicles
FCs	Fuel Cells
FESEM	Field Emission Scanning Electron Microscope
FWHM	Full Width at Half Maximum
GO	Graphene Oxide
HEV	Hybrid Electric Vehicles
HRTEM	High Resolution Transmission Electron Microscope
LIB	Lithium ion battery
LIBs	Lithium ion batteries
NPs	Nanoparticles
$Ni(OH)_2$-r-GO	Nickel hydroxide graphene composite
OCV	Open Circuit Voltage
SC	Supercapacitor
SCs	Supercapacitors

SEI	Solid Electrolyte Interphase
SEM	Scanning Electron Microscope
TEM	Transmission Electron Microscope
TGA	Thermo Gravimetric Analysis
XRD	X-ray Diffraction

List of figures

ABSTRACT

In the present thesis work, a single-step surfactant-free gram scale hydrothermal synthesis of mesoporous $Ni(OH)_2$ nanoparticles and the $Ni(OH)_2$-reduced graphene oxide ($Ni(OH)_2$-r-GO) nanocomposite. Interesting morphological features are noted. These nanomaterials are examined and compared as anode materials for pseudo-capacitor application through detailed characterizations. A high specific capacitance (C_s) of 1538 F/g is observed for $Ni(OH)_2$-r-GO at a high current density of 40 A/g, whereas at the same current rate bare $Ni(OH)_2$ shows C_s of only 936 F/g.

1.0 INTRODUCTION

1.1 Nanomaterials and Nanotechnology

Materials have been playing a tremendously vital role in the progress of human development since last many years [1]. The Nanoscience deals with materials of very small dimension usually in the range 1 to 100 nm. In an annual talk given by Nobel Laureate and American physicist Richard P. Feynman at the annual meeting of the American Physical Society (APS), at California Institute of Technology, entitled "There's Plenty of Room at the Bottom" [2]. He had described a vision to synthesize nanoscale building blocks with precisely controlled size and composition, and assemble them into larger structures with unique properties and functions. However the term "nanotechnology" was first coined in 1974 by Norio Taniguchi, then a professor of Tokyo Science University [3]. The essence of nanoscience and nanotechnology is the ability to understand, fabricate and engineer materials, devices and systems in the nanometer regime. The concepts and ideas derived from physics, chemistry, biology and engineering are merged together to design a novel material with desired properties. The properties and functionalities of the materials building blocks may be different as their size grows from the nano-regime to the micro regime and finally to bulk structures [4]. Nanotechnology is considered as an emerging technology with existing materials. The nanoscience is defined as the study of phenomena and manipulation of materials at atomic, molecular and macromolecular scales, when at least one of the dimension of materials usually in the range below 100 nm. The physical, chemical, mechanical, electronic, optical, magnetic, thermal etc. properties in this regime are dramatically different than the bulk material. Nanotechnologies deals with design, characterization, production and application of structures, devices and systems by controlling shape and size at the nanometer scale. The properties of materials can be different at the nano scale for two main reasons: First, nano materials have relatively larger surface to volume ratio. This can make materials more chemically reactive, and affect their strength or electrical properties. Second, the quantum effects begin to dominate behavior of matter at the nano-scale affecting optical, electrical and magnetic properties. Nanomaterials can be metals, ceramics, polymeric materials, or composite materials [5]. Nanomaterials have actually been produced and used by humans for hundreds of

2

years. Today, nanomaterials are being extensively explored for their application in energy storage and conversion.

1.2 Energy

Energy has two important aspects: generation and storage. As a consequence of ruthless exploitation of natural resources especially non-renewable sources of energy, today's developing society has us forced us to move towards sustainable and renewable sources of energy [6]. This has led to the tremendous increase in the efforts towards the development of devices and methods for the conversion of renewable sources of energy such as solar energy, wind energy, hydro energy etc. [7]. Significant amount of work has been done for harnessing solar as well as wind energy by using solar cells (silicon and dye solar cells) and wind mills respectively. Similarly, hydro energy has been exploited by building dams. However, solar energy is not available at night, wind is not available every time and hydrostatic potential energy of water is available with poor efficiency [8]. These challenges arising in the usage of renewable sources of energy demand robust and better energy storage devices [9].

The electrical energy can be stored using batteries and capacitors. In batteries electrical energy is generated by conversion of chemical energy through the redox reactions occurring at the anode and cathode. Capacitors store energy by the accumulation of charges at the two electrodes [10]. However, both these devices suffer from various disadvantages such as batteries cannot deliver power after a certain limit due to the limitation of the reaction kinetics. Capacitors on the other hand have high power density but they have limitations on the energy density. In order to address the issues confronted in energy storage, a new technology called 'Supercapacitors' has emerged with a potential to enable efficient energy storage. Supercapacitors work on the similar principles to that of capacitors but utilize higher electrode surface area and thinner dielectric to achieve higher capacitance values. This allows supercapacitors to possess higher energy and power density when compared to that of traditional capacitors [11]. These advantages make supercapacitors an attractive power solution to a number of applications. Supercapacitors are used in conjugation with LIBs in laptops, portable media players, power backup, hybrid electrical vehicles *etc.*[12].

3

1.3 Conventional Capacitors

A conventional capacitor consists of two conducting plates (electrodes) separated by an insulating dielectric material. When a voltage is applied across the two electrodes, opposite charges accumulate at the surface of the two electrodes. The dielectric prevents these charges from recombining and thus produces an electric field which allows the capacitor to store energy [13]. This phenomenon is illustrated in figure1.
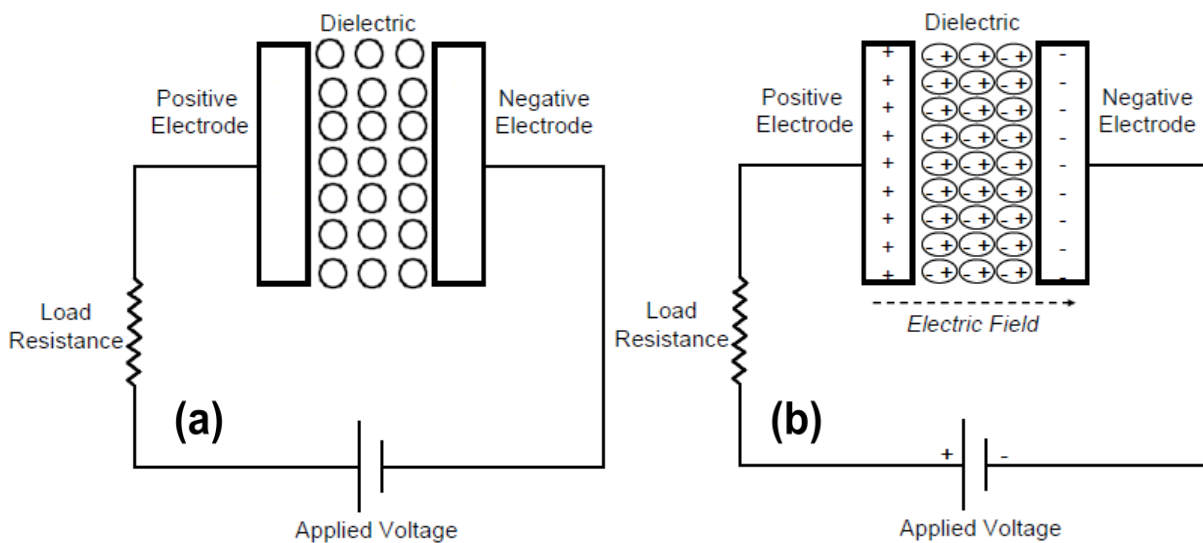
Figure1. Schematics of a conventional capacitor in its uncharged (a) and charged (b) state

The capacitance (C) is defined as the ratio of the charge stored (Q) to that of the voltage applied (V). The capacitance is given as:

$$C = \frac{Q}{V}$$

The capacitance is directly proportional to the surface area (A) of each electrode and inversely proportional to the distance (d) between the two electrodes. The capacitance is given as:

$$C = \varepsilon_o \varepsilon_r \frac{A}{d}$$

Where ε_o is the permittivity of free space and ε_r is dielectric constant of the insulating medium in between the two electrodes.

4

Generally, a capacitor is characterized by the following two properties (i) Energy Density and (ii) Power Density. Both the energy and power density can be expressed as a quantity per unit mass (gravimetric density) or per unit volume (volumetric density). Energy (E) stored in a capacitor is proportional to the capacitance (C) and voltage (V) across the two electrodes of the capacitor [14]. The energy is given as:

$$E = \frac{1}{2}CV^2$$

The Power (P) for a capacitor is defined as energy derived per unit from a capacitor. The maximum power that can be derived from a capacitor is given by the following relation:

$$P_{max} = \frac{V^2}{4 * R_s}$$

Where R_s is the equivalent series resistance (ESR), it is the combination of resistances from current collector, electrodes and dielectric material. The conventional capacitor has higher power density than that of batteries and fuel cells but it has low energy density.

1.4 Supercapacitors

In order to improve the energy density and capacitance of conventional capacitors concept of supercapacitor was introduced in mid twentieth century. Supercapacitors also utilize the concept of conventional capacitors but they incorporate electrodes with much higher surface area and a much thinner dielectric that reduces the distance between the two electrodes leading to the increase in the capacitance as well as energy. Figure 2 shows the schematic of a supercapacitor, representing its physical properties. Moreover, supercapacitors allow us to manipulate the E.S.R component thereby enabling us to achieve high power densities. In addition to high power and energy density supercapacitors also offer advantages of long cycleability, short charging time and low self discharge rate over electrochemical batteries [14]. The nature of application of energy storage technologies are determined by power and energy scales.
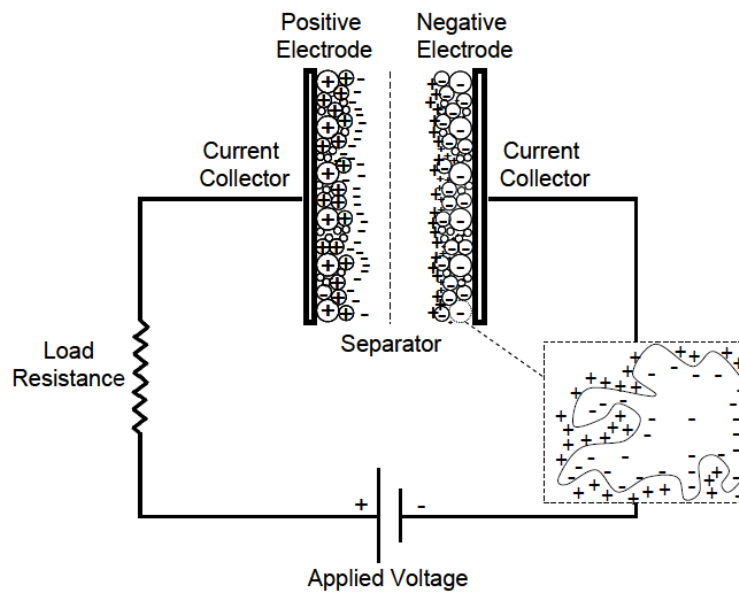
Figure 2. Schematic representation of an electrical double layer supercapacitor

(Adapted from Supercapacitors: A Brief Overview, M. S. Halper J. C. Ellenbogen)

The improvement in the performance of the supercapacitors and other energy storage devices is assessed with the help of Ragone plot [14]. It is plotted by measuring the energy densities and power densities of energy storage devices along the abscissa and ordinate axes respectively.
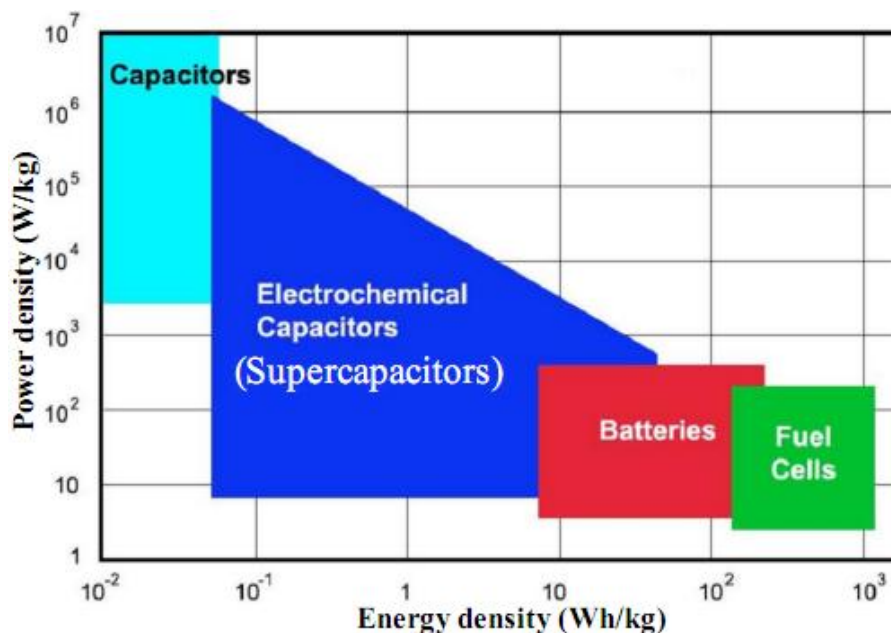
Figure 3. Ragone plot of various energy storage devices

(Adapted from http://www.seas.ucla.edu/~pilon/EES.html)

Figure 3 represents a Ragone plot. It can be observed from the plot that supercapacitors occupy a region between conventional capacitors and batteries.

Supercapacitors have higher energy density when compared to conventional capacitors and greater power density in comparison to batteries. These attributes of supercapacitors make them more adept to practical applications.

1.5 Classification of Supercapacitors

Supercapacitors can be classified into three major sub classes depending upon the mechanism of charge storage employed in the device [12]. The three major types of supercapacitors are as follows:

1. Electrical Double Layer Capacitors (EDLCs)
2. Pseudocapacitors
3. Hybrid Capacitors

The classification of supercapacitors is represented in the taxonomy tree in figure 4.
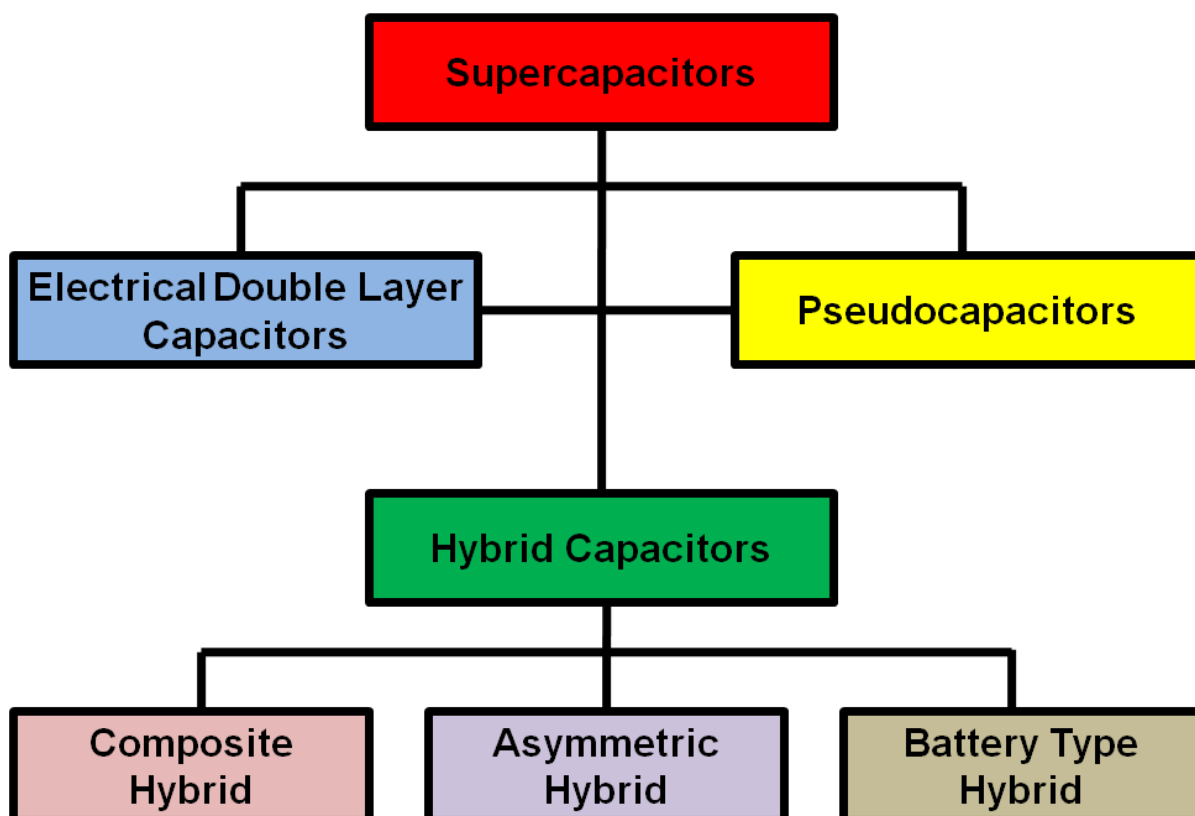
Figure 4. Classification of Supercapacitors

1.5.1 Electrical Double Layer Capacitors (EDLCs): EDLCs are constructed using two high surface area carbon electrodes, an electrolyte and a separator. The

schematic of an EDLC is shown in figure 2. The mechanism of charge storage in EDLC is similar to that of conventional capacitor. The charge storage here is achieved by separation of charges in a Helmholtz double layer at the interface between the electrode and the electrolyte, without involving any electron transfer from the electrode surface into the electrolyte or vice versa [9]. This mechanism of charge storage is also termed as Non-Faradaic charge storage. When the voltage is applied across the two electrodes of the EDLC, the diffusion of electrolyte ions towards electrodes of opposite polarity takes place. This leads to the charge accumulation at the electrode surfaces due to the electrostatic attraction between unlike charges present in the electrolyte and at the electrode. This result in the formation of electrical double layer at each electrode, allowing EDLCs to achieve higher energy densities compared to conventional capacitors. The performance of the EDLC depends upon the carbon material (activated carbon, carbon aerogels, carbon nanotubes etc.) and nature of electrolyte (aqueous or organic) used for the fabrication of the capacitor. EDLCs suffer from a limited theoretical capacity.

1.5.2 Pseudocapacitors: Pseudocapacitors are constructed with electrodes made up of metal oxides or conducting polymers. Pseudocapacitors store electrical energy through Faradaic reactions (redox reactions, intercalation and electrosorption) occurring, which is facilitated by electron charge transfer between electrode and electrolyte [8]. The Faradaic processes result in the attainment of higher capacitance and energy density for pseudocapacitors when compared to EDLCs.

1.5.3 Hybrid Capacitors: Hybrid capacitors are made up of two different electrodes, one of which has non-Faradaic (electrostatic) charge storage mechanism and the other has Faradaic (pseudocapacitive) charge storage mechanism [11]. Hybrid capacitors aim to exploit the advantages of both EDLCs and pseudocapacitors in order to achieve better performance with higher energy and power density. These are further sub divided on the basis of their electrode composition into three categories: composite, asymmetric and battery type hybrid capacitors.

(i) **Composite Hybrids:** The composite electrodes are composed of both carbon based materials and metal oxides enabling them to employ both physical and chemical mechanisms of charge storage together in a single

electrode. This leads to the better performance of the composite electrodes.

(ii) Asymmetric Hybrids: Asymmetric hybrid capacitors are constructed using one electrode of EDLC type and the other electrode of pseudocapacitive type. Generally, a carbon based electrode (EDLC) is used as cathode and a metal oxide electrode (pseudocapacitive) is used as anode in an asymmetric assembly. Thus, asymmetric hybrid capacitors combine both Faradaic and non-Faradaic charge storage mechanism and achieve comparatively higher energy and power densities to that of EDLC.

(iii) Battery Type Hybrids: The battery type hybrid capacitors are composed of one battery electrode and the second electrode is a supercapacitor electrode. The motive here is to achieve high energy and power density supercapacitors by clubbing together a high energy density battery electrode with a high power density supercapacitor electrode. This also offers an added advantage of less charging time due to supercapacitor electrode.

1.6 Motive of the present work

In order to address the challenges faced by the energy storage technology both carbonaceous and metal oxide based materials are being explored for enhancing the performance of the supercapacitors. Carbon based nanomaterials are being intensely investigated as electrode materials in EDLC. However, these materials exhibit relatively low specific capacitance (C_s) values than desired [12]. Metal oxides/hydroxides are being separately investigated as efficient electrode materials in pseudocapacitors. However, their performance is limited due to low operating potential window [9]. In comparison to the carbonaceous materials, metal oxides offer an advantage of easier and cost effective synthesis. Metal oxides such as MnO_2, Co_3O_4, RuO_2, NiO, $Ni(OH)_2$ etc. have very high theoretical capacitance values due to ultra fast and highly reversible redox reactions [15(a-d)]. It has been established that the specific capacitance and rate performance of such pseudocapacitive materials depends greatly upon the use of active material in the electrode during electrochemical performance, and the rates of electron and ion transmission [16]. However, these pseudocapacitive materials usually suffer from low energy storage

due to poor conductivity, low stability at high current rate, limited potential window, and less utilization of active material during electrochemical performance. Therefore, development of pseudocapacitive materials with high surface area, porosity and greater electronic conductivity is desired to achieve high energy storage [17(a, b)]. The problem of low operating potential window is being separately addressed by developing asymmetric supercapacitors because such devices can provide higher energy density than individual electrode components [18].

Amongst various pseudocapacitive materials $Ni(OH)_2$ has emerged as one of the most promising candidates with high theoretical specific capacitance value (2082 F/g within 0.5 V), low cost and easy processing [19]. To enhance the supercapacitor properties of bare $Ni(OH)_2$, carbon based materials such as activated carbon, carbon nanotubes and graphene have been incorporated [20(a, b)]. The outstanding electronic conductivity and high surface area of graphene has helped in the enhancement of electrochemical performance of $Ni(OH)_2$ [21(a, b)]. Hybrid with graphene also forms a conducting network by connecting individual $Ni(OH)_2$ nanostructures thereby facilitating the fast electron transfer between the active material and current collector. Also, stacking of graphene sheets is prevented due to the anchoring of $Ni(OH)_2$ nanostructures onto the graphene sheets resulting in an enhanced electrochemical performance of the composite. Tang et al. [18] have reported a capacitance of 3300 F/g for $Ni(OH)_2$-CNT based composite. Yang et al. [22] have reported a capacitance of 3152 F/g for electrodeposited $Ni(OH)_2$. Yan et al. [23] have reported a capacitance of 2194 F/g for $Ni(OH)_2$-graphene based composite. Although these results are quite interesting and impressive, they suffer from some disadvantages such as scalability in synthesis and fading capacity at high current densities that has prohibited their practical applicability [24]. Also, the employed synthesis methods, e.g. chemical vapour deposition, electro-deposition are expensive to implement. This calls for the use of easy and cost effective materials synthesis methods which can render similar or better levels of performance.

In this work, we report a single step bulk scale, surfactant free hydrothermal synthesis of mesoporous channelled $Ni(OH)_2$ nanoparticles and their composite with reduced graphitic oxide (r-GO). We call the composite as $Ni(OH)_2$-r-GO. The important highlights of the present work are as follows:

(i) The synthesis procedure demonstrated here is easy, cost effective, and highly scalable and can be used commercially.

(ii) The specific capacitance values obtained for $Ni(OH)_2$ and $Ni(OH)_2$-r-GO at low current density are fairly comparable to the recent reports (please see Table 1 in results and discussion section).

(iii) $Ni(OH)_2$-G performs exceptionally well at high current rates delivering a C_s of 1538 F/g at a high current density of 40 A/g.

(iv) Both these electrode materials show excellent cyclic stability. The composite shows more than 90% capacity retention after 1000 cycles.

(v) The composite exhibits high capacitance and has low ESR value, which makes it suitable for application in asymmetric supercapacitors.

Finally, the important outcome of the thesis work is summarized in the last chapter.

2. MATERIALS AND METHODS

2.1 Materials

All the chemicals used for the synthesis were analytical grade and commercially available from Merck Pvt. Ltd. and were used as received without further purification.

2.2 Synthesis of mesoporous Ni(OH)$_2$ nanoparticles

In a typical procedure for the synthesis mesoporous channelled Ni(OH)$_2$ nanostructures, solution of NiCl$_2$·6H$_2$O (0.33M) was prepared by dissolving NiCl$_2$·6H$_2$O (11.9 g) in deionized (D.I.) water (150 mL) to form a uniform clear solution. Then aqueous solution NaOH (2M, 75 mL) was added drop-wise to the above solution to form a Ni(OH)$_2$ suspension, which was stirred for 30 min. The light green Ni(OH)$_2$ suspension was filtered and washed with distilled water several times to remove Cl$^-$, Na$^+$ ions and other possible impurities. Subsequently, the filtered Ni(OH)$_2$, without drying was directly added to aqueous solution of NaOH (2.5M, 200 mL) under fierce stirring for 30 min. Then, the suspension was transferred into a 250 mL Teflon-lined stainless steel autoclave. The sealed autoclave was heated to and maintained at 160°C for 20 h in an electric oven and then air-cooled to room temperature. The resulting light green precipitate was collected by centrifugation, washed with de-ionized water and alcohol alternately several times until the filtrate pH became neutral. Finally, the product was dried in a vacuum oven at 60 °C for 12 h. The total yield obtained was 6.2 g.

2.3 Synthesis of Graphene Oxide

Graphene Oxide (GO) was prepared by the oxidation of graphite powder according to the modified Hummer's method [25]. In this procedure, 5 g of graphite powder and 3.75 g of NaNO3 were mixed in a round bottom flask. Then 375 mL concentrated H$_2$SO$_4$ was added under constant stirring in an ice bath. Subsequently 22.5 g of KMnO$_4$ was added to this slurry very slowly for more than about 1 h. The cooling was continued further for about 2 h. The ice bath was then removed and the mixture was allowed to stir for five days at room temperature. A brown color slurry was obtained. To this slurry 700 mL of 5 wt % H$_2$SO$_4$ aqueous solution was added over duration of more than about 1 h under stirring at 98°C. The resulting mixture was

once again subjected to additional stirring of 2 h. Then the heating was stopped and the flask was allowed to cool down to about 60 ⁰C. Finally 15 mL of 30 wt % H_2O_2 was added and the mixture was stirred for an additional 2 h at room. The product was purified by repeating the centrifugation cycle given below 15 times.[37] An aqueous solution of 3 wt% H_2SO_4/0.5 wt% H_2O_2 (2 Litre) was added to the GO cake obtained as stated above and the mixture was subjected to bath sonication for 30 mins. It was then centrifuged and the supernatant liquid was removed. The GO slab thus obtained was subjected to centrifugation three times with 3 wt % HCl (2 Liter) solution and one time with D. I. water. Acetone was added to the settled product for the removal of the remaining acid. Finally, the product was dried at 60 ⁰C.

2.4 Synthesis of Ni(OH)$_2$-r-GO

Ni(OH)$_2$-reduced graphene oxide (Ni(OH)$_2$-r-GO) composite was prepared using basically a similar approach as for the synthesis of mesoporous channelled Ni(OH)$_2$ nanostructures. Initially, GO (150 mg) was added in deionized water (150 mL). After that, the above mixture was ultrasonicated for 1h to get homogeneous dispersion of GO in water (1 mg/ml). Then, NiCl$_2$·6H$_2$O (11.9 g) was dissolved in the GO dispersion. Later, the same procedure was followed as for the synthesis of bare Ni(OH)$_2$. In *situ* reduction of GO into reduced graphene oxide (r-GO) takes place when heated in the basic medium.[26]

2.5 Preparation of pseudocapacitor electrodes

The electrodes for the electrochemical measurements were prepared by mixing the active material (Ni(OH)$_2$/Ni(OH)$_2$-r-GO), conducting carbon (Super P), and binder (Kynar) in the weight ratio of (75: 20: 5) in *N* -methyl pyrrolidone (NMP) solvent in an agate mortar homogeneously and coating on carbon fibre paper (Toray paper, Alfa Aesar). The slurry coated papers were directly used as electrodes for measuring electrochemical properties after drying at 80 °C for 10 h in an electric oven.

2.6 Electrochemical measurements

Cyclic voltammetry (CV) studies, galvanostatic charge-discharge measurements and electrochemical impedance analysis were carried out using a three-electrode system. Ni(OH)$_2$ and Ni(OH)$_2$-r-GO were used as working electrodes, Hg/HgO as reference electrode, and platinum strip as a counter electrode. Cyclic voltammetry

was carried using 2M aqueous KOH solution as the electrolyte, at different potential scan rates (2-100 mV/s). The potential window used in the measurement was from 0 to 0.65 V. Charging and discharging was carried out galvanostatically by varying the current density from 1 to 40 A/g over a potential range of $0 - 0.55$ V. Cyclic stability study was carried out by cyclic voltammetry at a constant scan rate of 10 mV/s up to 1000 cycles.

3. CHARACTERIZATION TECHNIQUES

3.1 X-Ray Diffraction

X-Ray Diffraction (XRD) is a technique used for understanding structural properties of materials. Information such as crystal structure, lattice parameters, crystallite size, defects and strains in the lattice etc. about the materials can be determined with the careful analysis of XRD data. For the X-Ray diffraction measurements, a collimated monochromatic beam of X-rays is made to be incident on the analyte at various angles (θ). After the X-rays strike the analyte they diffract, producing constructive diffraction patterns for certain angles corresponding to particular planes (h,k,l), which satisfy the Bragg's diffraction condition. Schematic representation of X-Ray diffraction technique is shown in Figure 5. Bragg's condition is satisfied if the path difference is the integral multiple of the wavelength of the X-ray used. Bragg's condition is given by

$$2dsin\theta = n\lambda$$

Where d is the interplanar distance between diffracting planes, θ is the angle of incidence of X-Ray, λ is the wavelength of the incident X-Ray and n is in an integer.
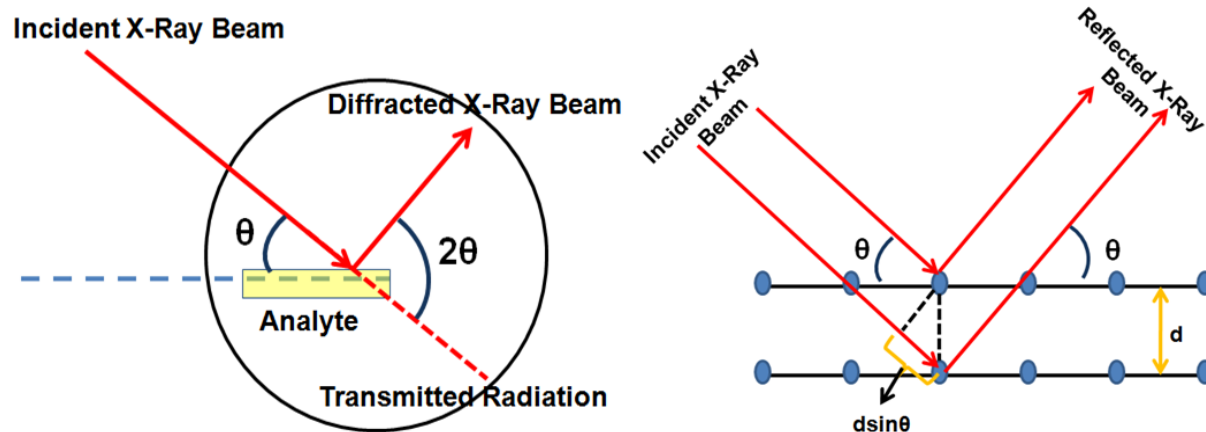
Figure 5 Schematics of X-ray diffraction technique

The samples were characterized for their phase purity and crystallinity with the help of XRD. The XRD measurements were carried out at room temperature using Philips X'Pert PRO instrument at Centre of Materials Characterization, National Chemical Laboratory (NCL) Pune.

3.2 Scanning Electron Microscopy

Scanning Electron Microscopy (SEM) is used for the analyses of surface and morphology of various nanostructures. It is used for the evaluation of grain size, surface roughness, porosity, particle size distribution, material homogeneity etc. In SEM, a focused electron beam is scanned across the surface of the sample that generates secondary electrons, backscattered electrons, and characteristic X-rays. These signals are collected by detectors to form images of the sample which are displayed on a cathode ray tube screen. The schematic representation of SEM is depicted in Figure 6.
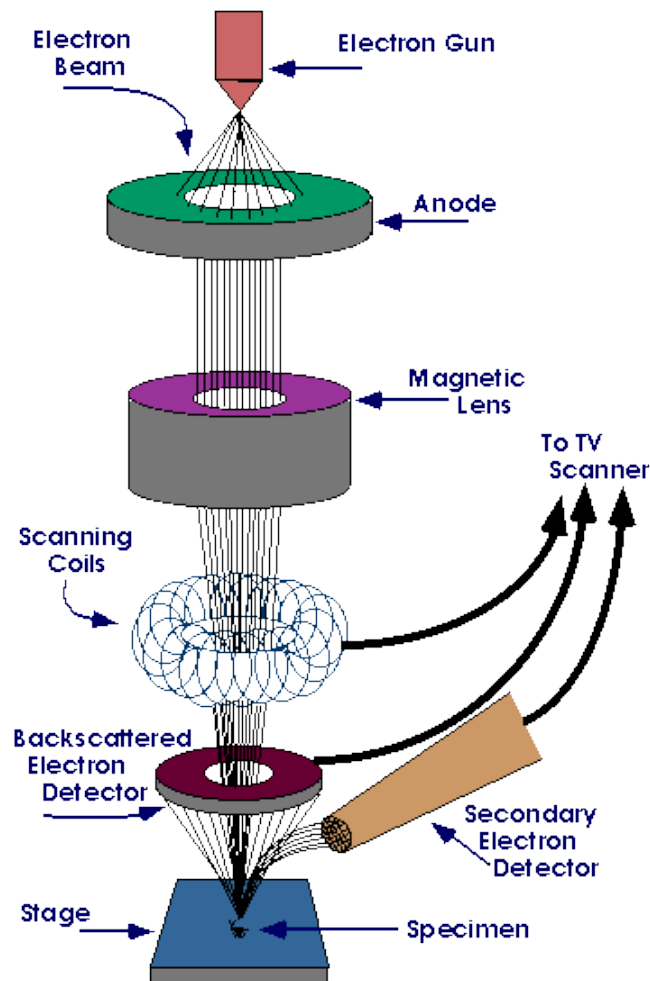
Figure 6. Schematic representation of Scanning Electron Microscope

(Adapted from http://www.purdue.edu/rem/rs/sem.htm)

The morphology of the prepared samples was analyzed using Nova NanoSEM 450 at NCL, Pune.

3.3 Transmission Electron Microscopy

Transmission Electron Microscopy (TEM) uses high energy electron beams to provide morphological, compositional and crystallographic information of the samples [27]. In TEM, a beam of high energy electrons is focussed on the sample. These electrons interact with the sample and get transmitted through it. The transmitted electrons are collected by the detector to form image on the fluorescent screen. The schematics of TEM are represented in figure7. Morphological details and particle sizes were investigated by TEM. TEM was performed on a FEI Technai 30 system microscope operated at 300 kV and 119 μA. The samples were drop-casted on a carbon coated copper grid after dispersing nanoparticles in deionized water.

Figure 7. Schematic representation of Transmission Electron Microscope

(Adapted from http://www.hk-phy.org/atomic_world/tem/tem02_e.html)

3.4 Energy Dispersive X-Ray Spectroscopy.

Energy Dispersive X-Ray Spectroscopy (EDS) is an analytical technique used for elemental analysis on chemical composition on mapping. It is generally coupled with SEM and TEM. During the Energy Dispersive X-Ray Analysi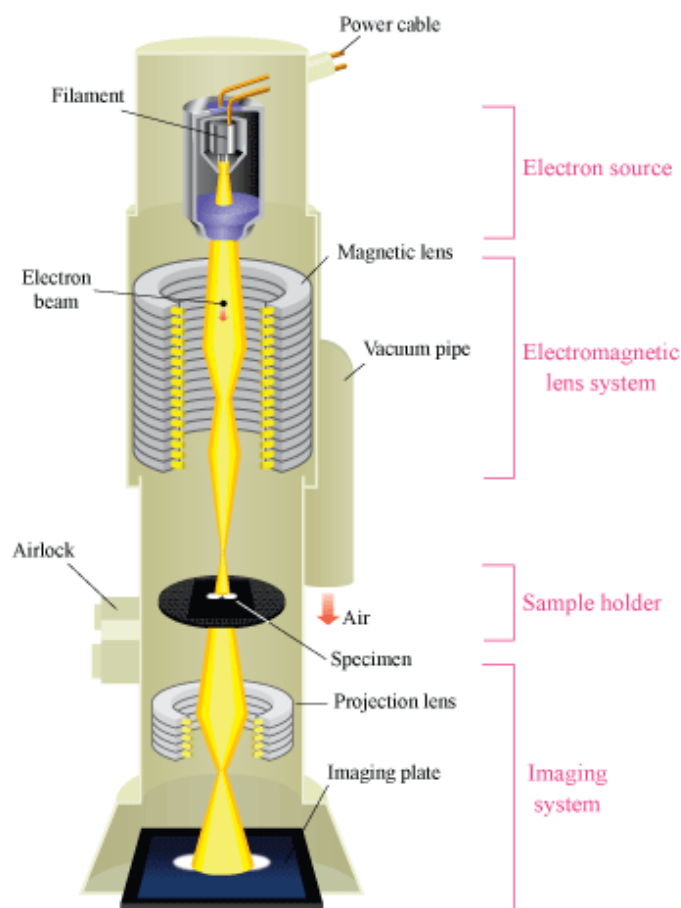s (EDAX) the sample is exposed to high energy electron beams. This stimulates the emission of characteristic X-rays from the sample. X-rays are produced when an inner shell electron is knocked off by electron beams; a higher energy outer shell electron fills the hole, releasing a quantum of energy in the form of X-rays. Energy of the X-rays is characteristic of the element from which they are emitted. The schematics of Energy Dispersive X-Ray Spectrometer are shown in figure 8. EDS was performed on the samples to study the elemental composition using an inbuilt Energy Dispersive X-Ray Spectrometer in Nova NanoSEM 450.

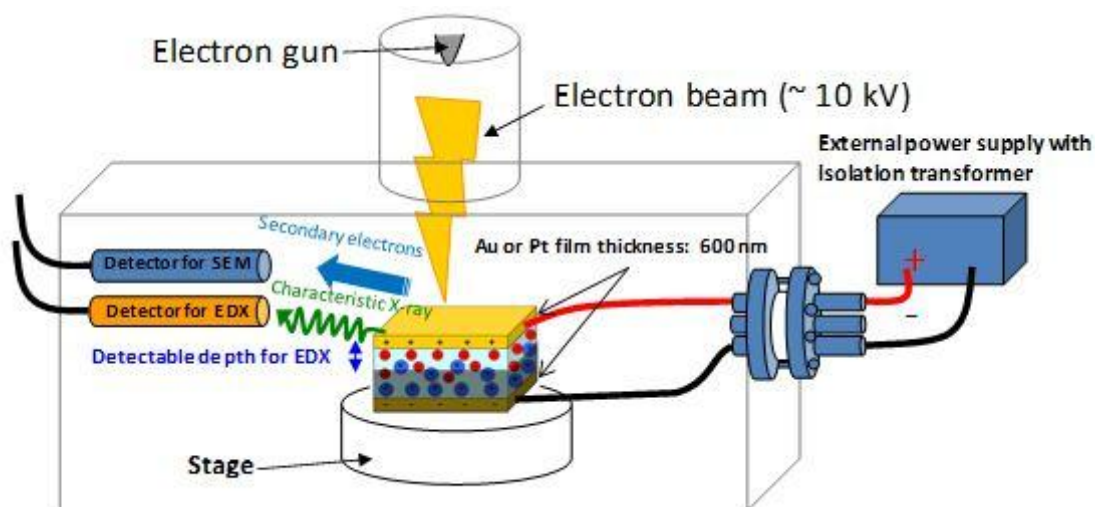**Figure 8. Schematic representation of Energy Dispersive X-Ray Spectrometer**

(Adapted from http://www.intechopen.com/books/ionic-liquids-new-aspects-for-the-future/use-of-ionic-liquid-under-vacuum-conditions)

3.5 Diffused Reflectance Spectroscopy

Diffused Reflectance Spectroscopy (DRS) is used to measure the characteristic reflectance spectra produced by a material when light is passed through it. The

spectrum obtained contains information about the optical properties and structure of the material being measured. It is generally used to find out the band gap and absorption maxima of optical materials which are not dispersible in any solvent and thin films. DRS measurements were performed using a Jasco V-570 spectrophotometer in order to confirm the presence of graphene in the composite. Spectra were taken, over the wavelength range 200-800 nm, circular compacts of test materials against a $BaSO_4$ compact (a product of Shimadzu Corp.) used as a totally reflective reference material.

3.6 Thermogravimetric Analysis

Thermogravimetry (TG) is used to analyze the thermal stability of materials under a variety of conditions. In Thermogavimetric Analysis (TGA), physical and chemical properties of materials are measured as a function of increasing temperature (with constant heating rate). TGA can provide information about the chemical processes such as decomposition, desolvation, dehydration etc. It can also provide information about the physical processes such as sublimation, vapourization etc. In the present study TGA was performed to estimate the amount of graphene present in the composite.

3.7 Brunauer–Emmett–Teller Surface Area Analysis

Brunauer–Emmett–Teller (BET) theory is used to explain the physical adsorption of gas molecules on a solid surface and it is exploited in finding out the surface area and pore size distribution of porous materials. BET analysis gives us the precise specific surface area of materials by measuring the multilayer adsorption of nitrogen as a function of relative pressure. The schematic of BET surface area analyzer is shown in figure 9. The technique encompasses external area and pore area evaluations to determine the total specific surface area in m^2/g yielding important information in studying the effects of surface porosity and particle size in many applications. In this work, BET analysis was carried out to confirm the porous nature of material and reason out the better capacitive performance of the materials prepared. The BET measurements were performed using N_2 adsorption – desorption isotherm in a Quantachrome (Nova 3200 e) surface area and pore size analyzer.
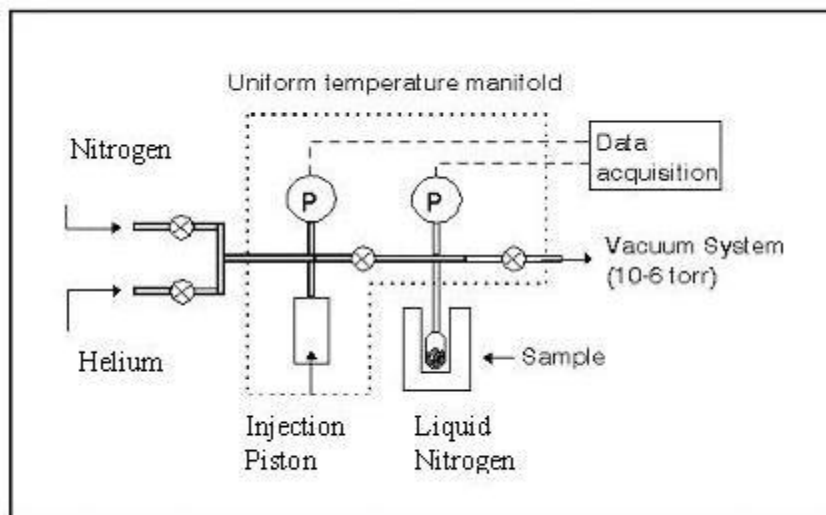
Figure 9. Schematic layout of BET surface area analyzer

(Adapted from http://saf.chem.ox.ac.uk/operating-principles-3.aspx)

3.8 Raman Spectroscopy

Raman spectroscopy is a technique used to observe low frequency modes in a system such as vibrational and rotational modes. In Raman spectroscopy a sample is generally illuminated with a laser beam in the ultraviolet (UV), visible (Vis) or near infrared (NIR) range. The laser light interacts with molecular vibrations, phonons or other excitations in the system, resulting in the energy of the laser photons being shifted up or down. The shift in energy gives information about the vibrational modes in the system. Scattered light is collected with a lens and is sent through interference filter or spectrophotometer to obtain Raman spectrum of a sample. Figure 10 shows the schematic representation of Raman spectrophotometer. Raman spectra are like the finger prints of materials. In the present work Raman spectroscopy was used to characterize $Ni(OH)_2$ and to establish the presence of graphene in the composite. The Raman spectroscopy was performed using a confocal micro-Raman spectrometer LabRAM ARAMIS Horiba Jobin-Yvon apparatus with laser excitation wavelength of 532 nm.

20
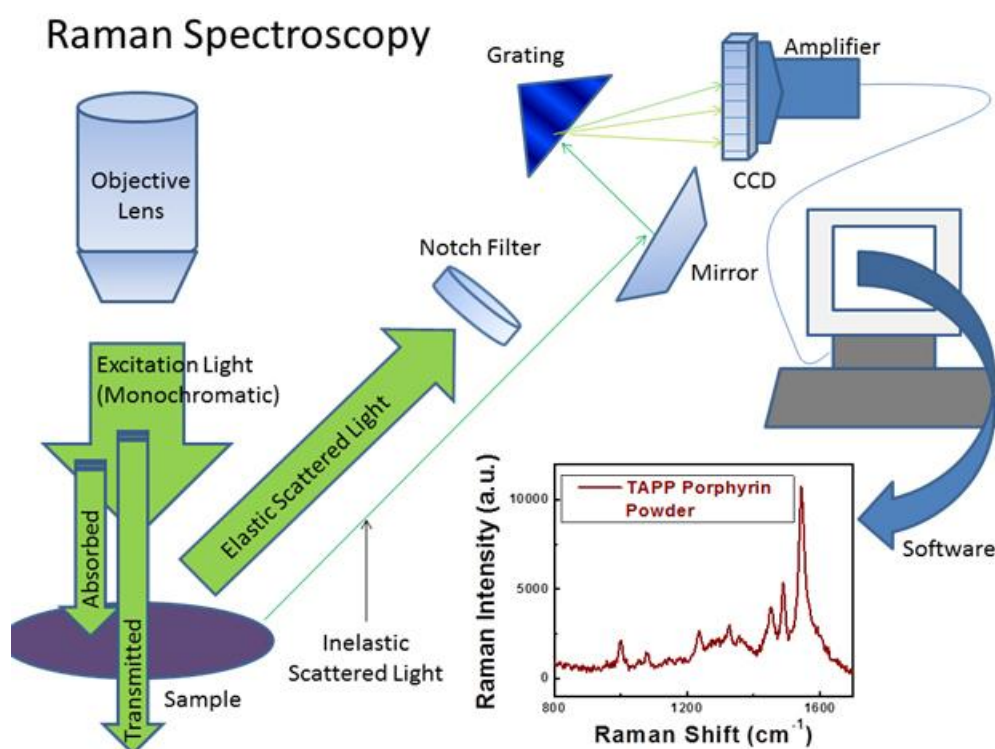
Figure 10. Schematic outlay of a Raman Spectrophotometer

(Adapted from http://www3.nd.edu/~kamatlab/facilities_spectroscopy.html)

3.9 Cyclic Voltammetry

When cyclic voltammetry reaches a set potential, the working electrode's potential ramp is inverted. This inversion can happen multiple times during a single experiment. The current at the working electrode is plotted versus the applied voltage to give the cyclic voltammogram trace.

In this case the voltage is swept between two values at a fixed rate. However, now when the voltage reaches V_2 the scan is reversed and the voltage is swept back toV_1. A typical cyclic voltammogram (figure 11) recorded for a reversible single electrode transfer reaction is shown in below. In cyclic voltammetry, the electrode current versus applied potential is represented. The ramping is known as the experiment's scan rate (V/s). The potential is applied between the reference electrode and the working electrode and the current is measured between the

working electrode and the counter electrode. These data are then plotted as current (i) vs. potential (E).
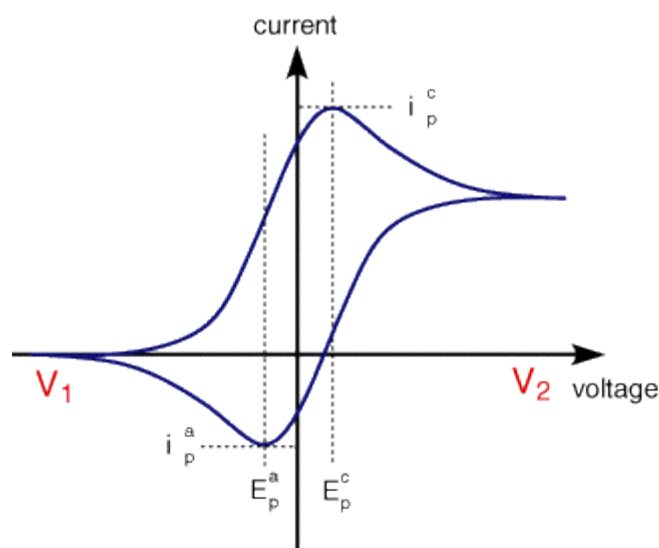
Figure 11. A typical cyclic voltammogram

(Adapted from http://www.ceb.cam.ac.uk/pages/linearsweep-and-cyclic-voltametry-the-principles.html)

As shown in figure 11, the forward scan produces a current peak for any analytes that can be reduced (or oxidized depending on the initial scan direction) through the range of the potential scanned. The current will increase as the potential reaches the reduction potential of the analyte, but then falls off as the concentration of the analyte is depleted close to the electrode surface. If the redox couple is reversible then when the applied potential is reversed, it will reach the potential that will reoxidize the product formed in the first reduction reaction, and produce a current of reverse polarity from the forward scan. This oxidation peak will usually have a similar shape to the reduction peak. As a result, information about the redox potential and electrochemical reaction rates of the compounds is obtained. Cyclic Voltammetry provides a wide range of information about the electrode and electrode/electrolyte interaction and the nature of the cyclic voltammogram depends upon the types of measurements for desired applications.

3.10 Galvanostatic Charge Discharge for capacitance and stability measurement

Cyclic charge discharge is a standard galvanostatic technique that is used to test the performance and cycle-life of supercapacitors and batteries. A repetitive loop of charging and discharging is called a cycle. Charge and discharge analysis are conducted at constant current rate until a set voltage is reached. For aqueous electrolyte the potential window is (0-1V) whereas for non aqueous electrolytes it is (0-3V). The curve provide charge and discharge time for capacitor from which the capacitance and stability is calculated. The capacitance is calculated using the following equation:

$$C_s = \frac{I * \Delta t}{m * \Delta V}$$

Where, C_s is specific capacitance (F/g), I is current (A), Δt is discharge time(s), m is the mass of active material (g) and ΔV is potential drop during discharge (V). The cyclic voltammetry and other electrochemical characterisations were done on AutoLab PGSTAT 30, eco-chemie.

4.0 RESULTS AND DISCUSSION

X-ray diffraction patterns of the $Ni(OH)_2$ and $Ni(OH)_2$-r-GO composite samples are shown in figure 12. All the peaks of $Ni(OH)_2$ match very well with the PCPDF data file No. 140117 (hexagonal primitive lattice). The presence of sharp peaks in the $Ni(OH)_2$ and the $Ni(OH)_2$-r-GO composite confirms the good crystalline nature of the hydroxide phase in both the cases.
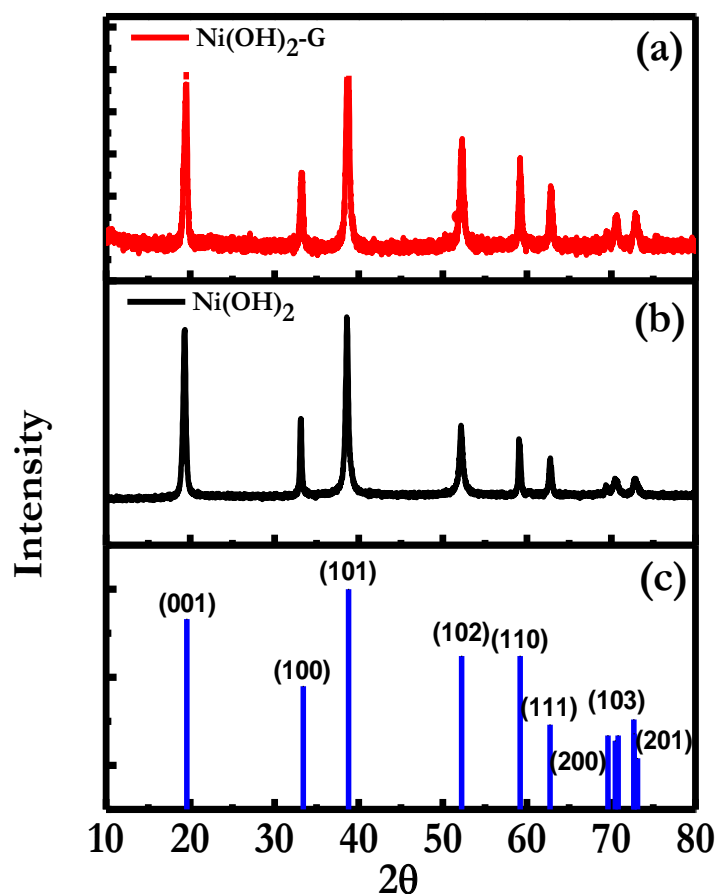
Figure 12. XRD patterns for (a) $Ni(OH)_2$-r-GO composite, (b) $Ni(OH)_2$, and (c) $Ni(OH)_2$ (PCPDF standard data)

Moreover, no extra peaks are observed confirming the high purity of the phase. In the case of the composite involving hydroxide of high Z element Ni the r-GO contribution is not easily discernible due to its low content, and the low Z of carbon. In order to reveal the presence of r-GO more clearly we dissolved the $Ni(OH)_2$ component of the composite with concentrated HCl. The resulting product gave an XRD as shown in figure 13(a). The occurrence of a broad hump around 2θ value of 23-26° unambiguously represents r-GO, implying that we do have r-GO in our composite phase. Moreover, no peak is observed around 2θ value of 10º

24

(present in GO) which confirms the successful reduction of GO to r-GO during the synthesis of the composite.

To further confirm the presence of r-GO in the composite Raman spectroscopy was performed on the sample obtained by dissolving the hydroxide from the composite.
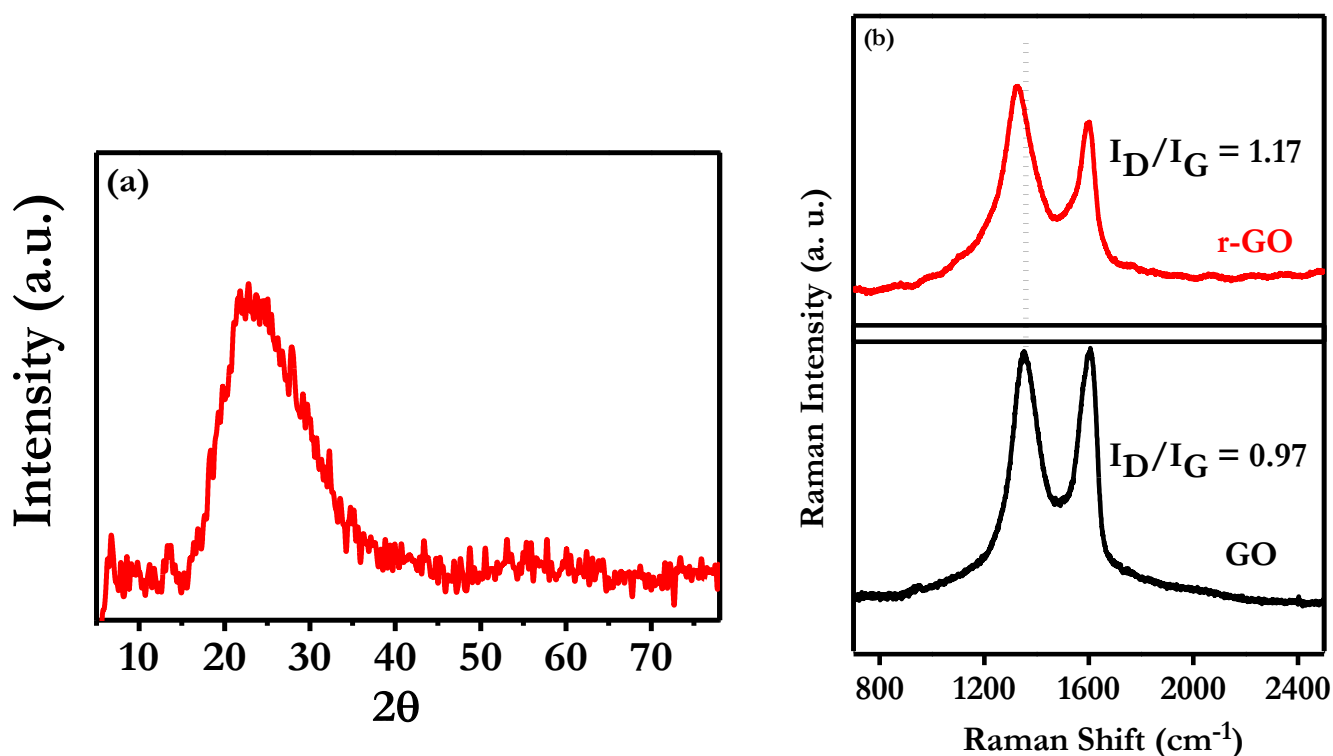
Figure 13. (a) XRD spectrum of r-GO obtained from Ni(OH)₂-r-GO by dissolution of hydroxide, (b) Raman spectra of GO used for the synthesis of composite and r-GO obtained from Ni(OH)₂-r-GO by dissolution of the hydroxide

Figure 13(b) shows the Raman spectrum for this sample along with the spectrum for GO which was used as the starting material during the synthesis of the composite. Raman spectra reflect the reduction of GO to r-GO via the changes in relative intensity of the two main peaks: D and G [28]. Also, there is considerable shift of the D peak towards lower wave number as expected for the GO to r-GO transformation. The D band originates from the defect-induced breathing mode of sp^2 rings [29] and arises from the stretching of C-C bond. The G peak on the other

hand is due to the first order scattering of the E_{2g} phonon of sp^2 C atoms [30]. The intensity of the D band depends on the size of the in-plane sp^2 domains [30] and its increase indicates formation of more sp^2 domains. The relative intensity ratio (I_D/I_G) reflects the degree of disorder and is inversely proportional to the average size of the sp^2 clusters. In our case the I_D/I_G ratio for GO used as the starting material is 0.97 while that for the carbon obtained after hydroxide dissolution is 1.17. This increase in the intensity ratio implies that newer graphene domains are formed and the sp^2 cluster number is increased [34] after composite formation process. This supports the conclusion that we have a $Ni(OH)_2$-r-GO composite.

In order to further confirm the presence of r-GO in the composite Diffuse Reflectance Spectroscopy (DRS) was performed on the samples. The DRS spectra of the $Ni(OH)_2$ and its r-GO based composite are shown in figure 14.
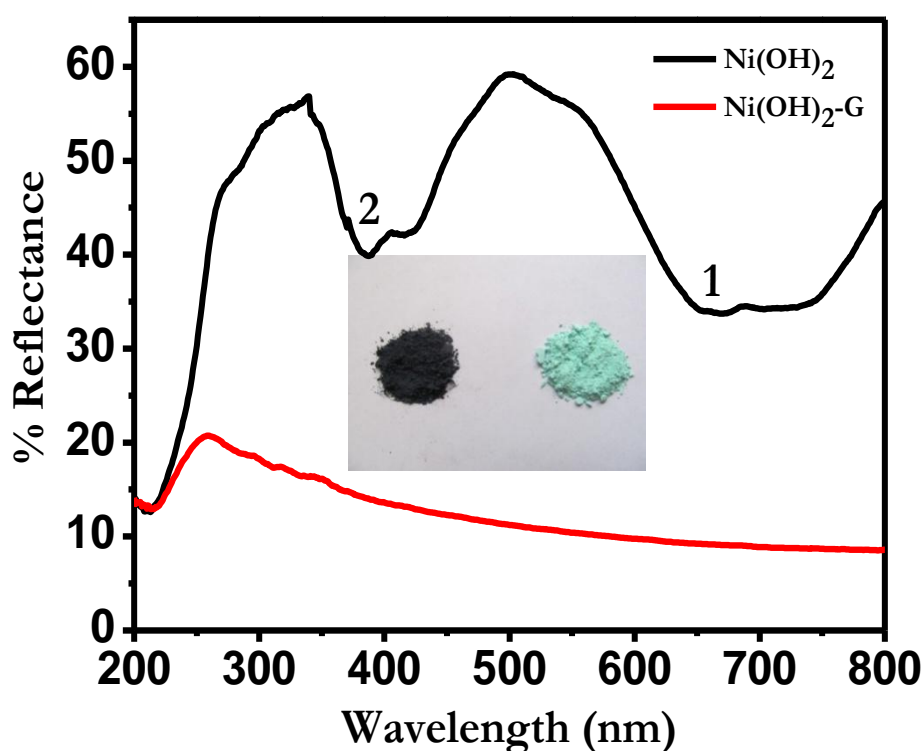
Figure 14. DRS spectra of Ni(OH)$_2$ and Ni(OH)$_2$-r-GO composite. Inset image shows the color of the bare Ni(OH)$_2$ (green) and the Ni(OH)$_2$-r-GO (black) composite

The absorbance at 655 nm (marked as 1 in the figure) and 380 nm (marked as 2 in the figure) are the d-d transitions of Ni^{2+} in octahedral coordination arising due to $^3A_{2g} \rightarrow {}^3T_{1g}$ and $^3A_{2g} \rightarrow {}^3T_{2g}$ transitions respectively. The DRS spectrum of bare

Ni(OH)$_2$ matches with the previous literature report [31]. The spectrum of Ni(OH)$_2$-r-GO shows a much higher absorbance when compared to bare Ni(OH)$_2$ and the signature peaks for Ni^{2+} are not visible due to the presence of r-GO. The inset to Figure 14 shows the images of Ni(OH)$_2$ and Ni(OH)$_2$-r-GO. The bare Ni(OH)$_2$ is green in color whereas Ni(OH)$_2$-r-GO appears blackish due to the presence of r-GO.

Thermal behavior of the samples was also investigated using Thermogravimetric Analysis (TGA). Figure 15 shows the TGA plots for both Ni(OH)$_2$ and Ni(OH)$_2$-r-GO. It can be seen from the TG curves that both of them begin to decompose at 230°C and the process is complete at 295°C. This decomposition is associated with the following reaction:

$$\text{Ni(OH)}_2 \rightarrow \text{NiO} + \text{H}_2\text{O}$$
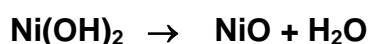
Further weight loss in the case of the composite can be attributed to the oxidation of r-GO to gaseous forms such as CO or CO$_2$. From the comparative study of weight loss it can be concluded that around 2 wt.% of r-GO is present in the composite. The TGA data thus further confirm the presence of r-GO in the composite.
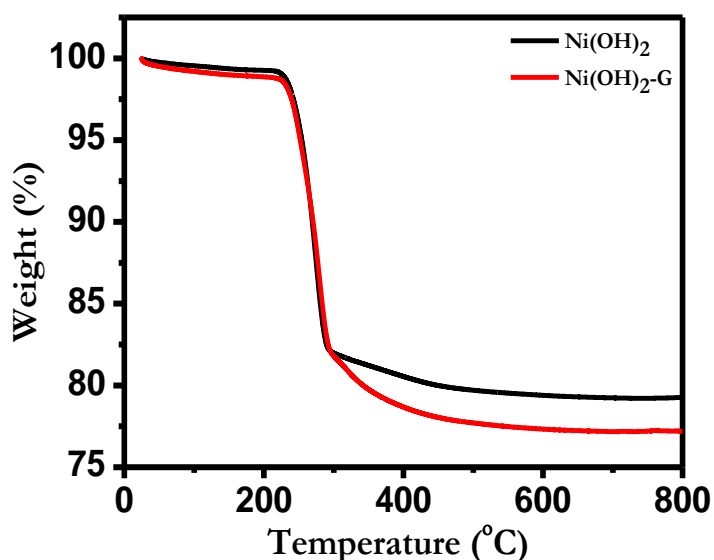

Figure 15. TGA of Ni(OH)$_2$-r-GO and Ni(OH)$_2$.

The specific area and pore size distribution of Ni(OH)$_2$-r-GO and bare Ni(OH)$_2$ were studied using the N$_2$ adsorption and desorption isotherms represented in figure

16. The specific surface area of bare $Ni(OH)_2$ is only 24.842 m²/g whereas that of the $Ni(OH)_2$-r-GO composite is 43.752 m²/g.
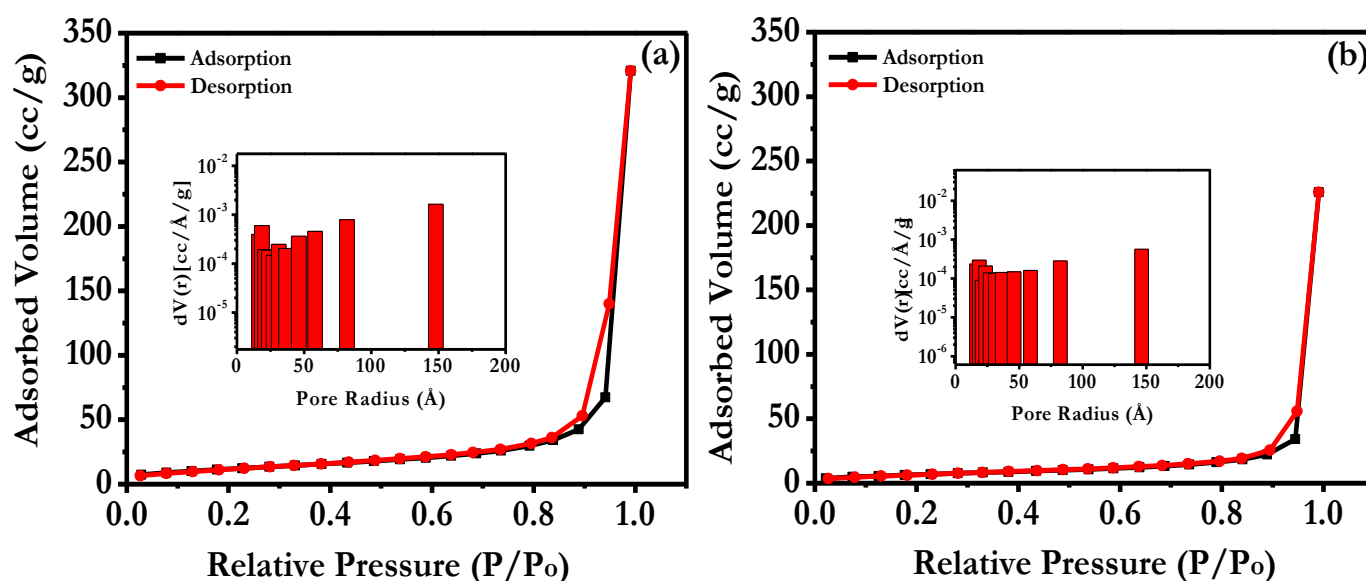
Figure 16. Adsorption-desorption isotherm and the pore size distribution (inset) for (a) $Ni(OH)_2$-r-GO and (b) $Ni(OH)_2$

This increase in the specific surface area of the composite can be attributed to the addition of r-GO that acts as an anchor for $Ni(OH)_2$ nanoparticles thereby avoiding the stacking of these nanoparticles. It is seen from the adsorption-desorption isotherm that at low relative pressure the adsorbed volume does not increase rapidly, indicating the presence of fewer number of micropores in the sample. However, as the relative pressure increases, the adsorbed volume increases and at high relative pressure small hysteresis loop is observed, which a characteristic of Type-V isotherm is. The presence of hysteresis loop indicates the presence of mesoporosity in the samples [32a]. Due to the capillary condensation in the mesopores, there is an increase in the adsorption isotherm in the relative pressure region of 0.4 to 0.8. The hysteresis loop observed here is the Type H3 loop, which does not represent any limiting adsorption at high relative pressures [32b]. This kind of loop is observed for slit-shaped pores in aggregated plate-like particles. The hysteresis loop in the case of our composite is bigger when compared to bare $Ni(OH)_2$. The inset of the Figure 5 represents the pore size distribution present in the samples. It is evident from the figure that distribution of pores in both the samples is

28

similar and predominantly mesoporous in nature, supporting the inference from the isotherm. However, it is observed that the pore volume in case of Ni(OH)$_2$-r-GO composite is relatively higher which relates to the fatter hysteresis loop and higher surface area (double).

Figure 17 shows the FE-SEM analysis for Ni(OH)$_2$-r-GO (a-c) and Ni(OH)$_2$ (d-f). The presence of different faceted structures for Ni(OH)$_2$ in both the samples can be easily observed (please see Figure 17 a and d). The morphology is mainly dominated by hexagonal plates. In the case of Ni(OH)$_2$-r-GO also, the basic morphology is similar. In order to confirm the presence of r-GO we drop-casted the composite solution on conducting silicon substrate to perform the elemental mapping analysis. The map shown in Figure 17b shows the overlay of nickel (Ni), oxygen (O) and carbon (C).
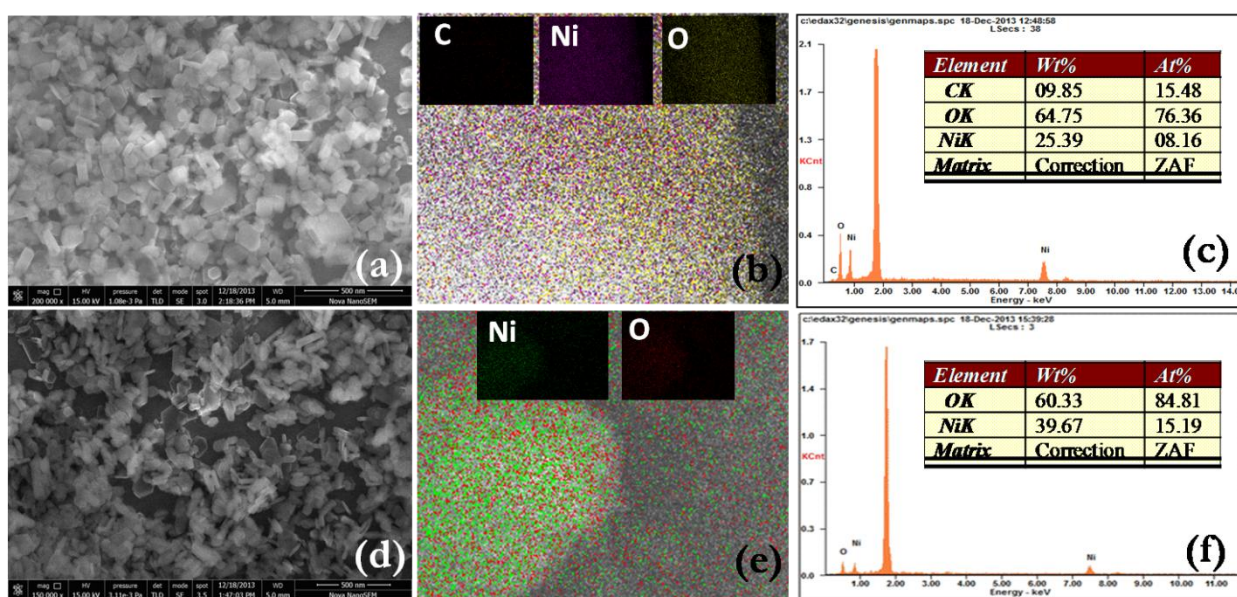
Figure 17. SEM image, elemental map, and energy dispersive x-ray analysis (EDAX) data for (a-c) Ni(OH)$_2$-r-GO and (d-f) Ni(OH)$_2$

The inset of Figure 17b shows the elemental maps of individual element present in the sample, confirming their uniform distribution in the Ni(OH)$_2$-r-GO composite. Energy dispersive analysis of x-rays (EDAX) spectrum for Ni(OH)$_2$-r-GO is depicted in Figure 17c. Figure 17(d-f) show the FE-SEM image, elemental mapping, and

EDAX spectrum for the bare Ni(OH)$_2$ sample for comparison. No carbon contribution is seen, as expected.

Figure 18 shows the TEM images for the Ni(OH)$_2$ and Ni(OH)$_2$-r-GO samples. Figure 18a clearly shows the presence of r-GO with hexagonal and elongated rod-like structures of Ni(OH)$_2$. The image also shows the interconnected nickel hydroxide nanoparticles on r-GO sheets along with the mesoporous channels. These kinds of mesoporous channels are very useful for charge storage applications as they can decrease the ionic diffusion length and also the electrolyte resistance.

Figure 18. HRTEM images for (a, b) Ni(OH)$_2$-r-GO and (c,d) Ni(OH)$_2$

Figure 18b shows the HR-TEM image of Ni(OH)$_2$-r-GO with interplanar distance of 0.23 nm, corresponding to (101) plane of Ni(OH)$_2$. Figure 18c shows the

image for bare $Ni(OH)_2$ which reveals porous hexagonal as well as elongated structures. The observed interplanar distance for bare $Ni(OH)_2$ is 0.24 nm (Figure 18d).

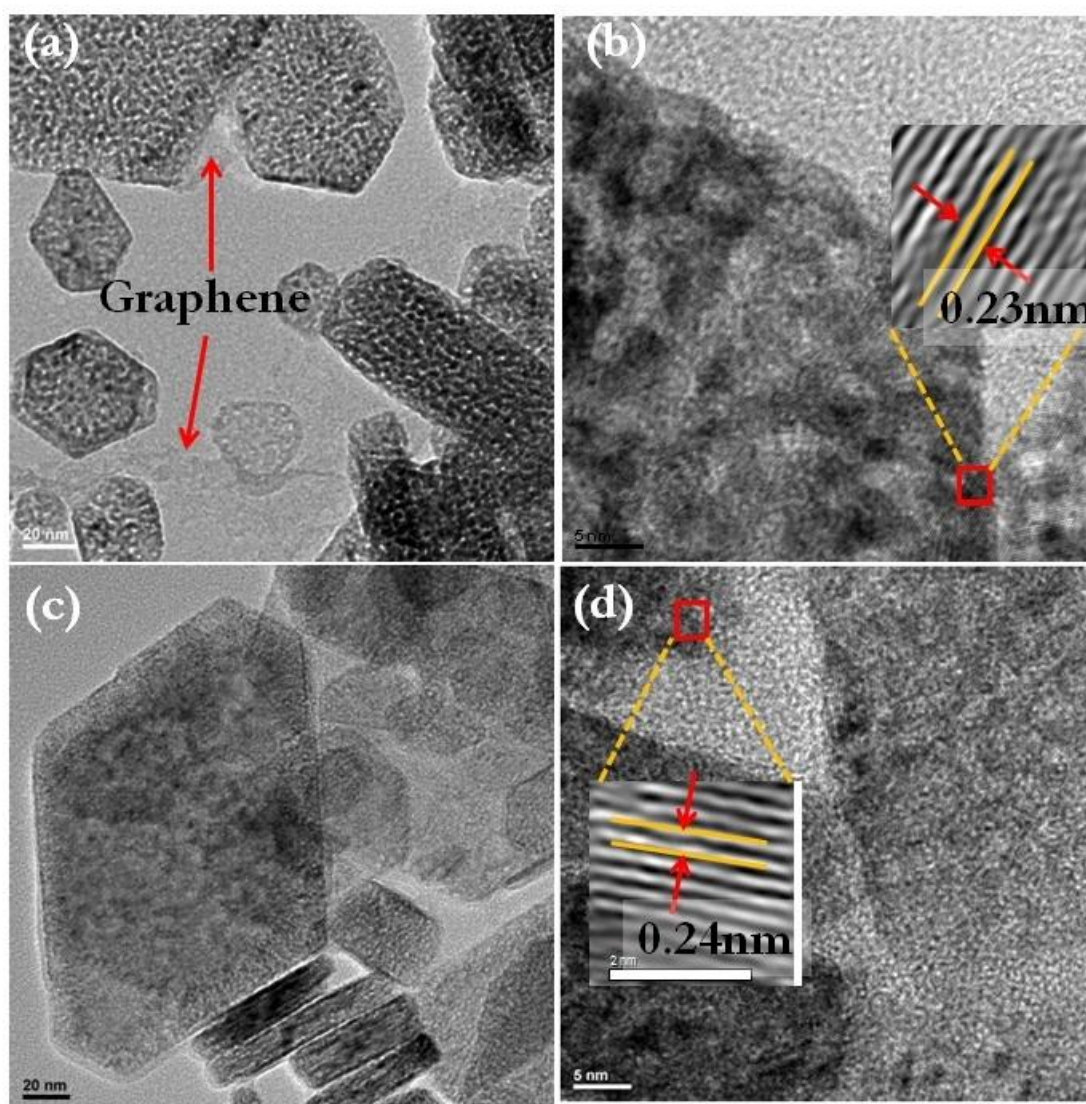From the data derived from the above characterizations, it is clear that these mesoporous channel based $Ni(OH)_2$ and $Ni(OH)_2$-r-GO can be useful in pseudo - capacitive charge storage. To find out the detailed electrochemical charge storage properties, we measured the cyclic voltamogram (CV) in three electrode assembly in 2M KOH with platinum and mercury-mercury oxide (Hg/HgO, 30% KOH) as counter and reference electrodes, respectively. Figure 19 a and b represent the CV for $Ni(OH)_2$-r-GO and $Ni(OH)_2$, respectively. The CV was performed at different scan rates from 2 to 100 mV/s. Since $Ni(OH)_2$ is known to be a good anode material in supercapacitor performance, the cyclic voltammetry was carried out by applying positive potential with respect to the reference electrode. During sweep, the potential window range was selected in such way as to avoid strong polarization due to water splitting issue. The CV curve in both the cases shows two distinct, ideal, and symmetric oxidation-reduction peaks.
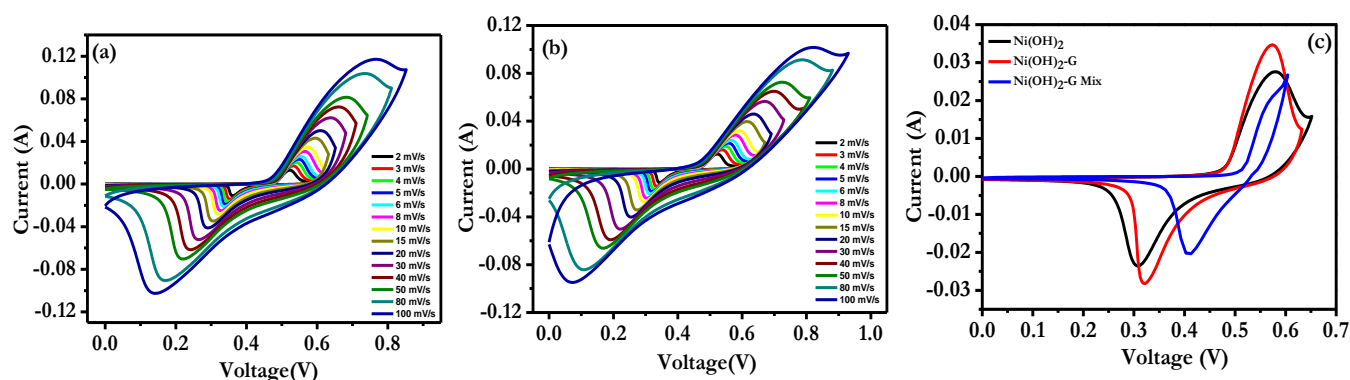
Figure 19. Cyclic voltametry (CV) at different scan rates from 2 to 100 of mV/s for (a) $Ni(OH)_2$-r-GO, (b) $Ni(OH)_2$, (c) The CV plot comparision between $Ni(OH)_2$-r-GO and $Ni(OH)_2$ at the scan rate of 10 mV/s

From the CV signatures it is very clear that the charge storage contribution is only through Faradaic reactions. This confirms the pure pseudocapacitive nature of $Ni(OH)_2$. The oxidation and reduction peaks originate from the following reversible reaction.

$$\text{Ni(OH)}_2 \rightleftharpoons \text{NiOOH} + e^-$$

In both the samples under study, on increasing the scan rate from 2 to 100 mV/s, the oxidation peaks shift towards the right and the reduction peaks shift towards the left. This is very common for metal oxide based materials having low surface area and it is mainly due to the diffusion resistance of the ions at the high scan rates. Symmetric oxidation and reduction peaks observed at low scan rate (2 mV/s) are even maintained at a very high scan rate (100 mV/s) for both the electrodes Figure 19 (a, b). This proves high rate performance of these materials.

Figure 19c compares the CV plots for the Ni(OH)$_2$, Ni(OH)$_2$-r-GO and the physical mixture of r-GO and Ni(OH)$_2$ (comparable composition ratio of constituents) samples with same mass loading and scan rate of 10 mV/s. The peak current is significantly less for the physical mixture when compared with bare Ni(OH)$_2$ and composite. There are three major differences which are very important to notice. First, the oxidation and reduction peak current value in the Ni(OH)$_2$-r-GO case is much higher than that for bare Ni(OH)$_2$, which yields higher C_s value for the composite. Second, the oxidation and reduction peaks of Ni(OH)$_2$-r-GO are sharp whereas the peaks for only Ni(OH)$_2$ case are relatively broad in nature. This is mainly because of higher porosity and surface area which gives faster ion transport into the electrode (decreasing the diffusion path length of the electrolyte) in the case of Ni(OH)$_2$-r-GO as compared to Ni(OH)$_2$. The role of r-GO cannot be neglected here as it gives electrical conductive channel for electrons consumed or generated by the Faradaic reactions on the Ni(OH)$_2$ surfaces, and it also provides the high surface area and better accessibility for the electrolyte. Third is the observation of more reversible nature of Ni(OH)$_2$-r-GO as compared to the Ni(OH)$_2$ electrode. The potential difference between the oxidation and reduction peaks for Ni(OH)$_2$-r-GO (0.25 V) is less than that for Ni(OH)$_2$ (0.27 V). Thus, the Ni(OH)$_2$-r-GO electrodes offer kinetically smaller barrier for redox reactions over bare Ni(OH)$_2$.

From the points discussed above, the superiority of the Ni(OH)$_2$-r-GO electrodes in electrochemical charge storage over Ni(OH)$_2$ is clearly revealed. To calculate the gravimetric capacitance, galvanostatic charge-discharge measurements for both the electrode materials were performed in 2M KOH solution using three electrode configuration by varying the current density from 1 to 40 A/g.

The discharge plots for both the cases are shown in Figure 20 (a, b). It is worth mentioning that the initial 200 cycles were required for both the electrodes to get stabilized (current density increases with cycling). Hence the charge discharge measurements were carried out after stabilizing the electrodes for 200 cycles. The observed long discharge plateau in both the cases confirms the Faradaic nature of these electrodes.
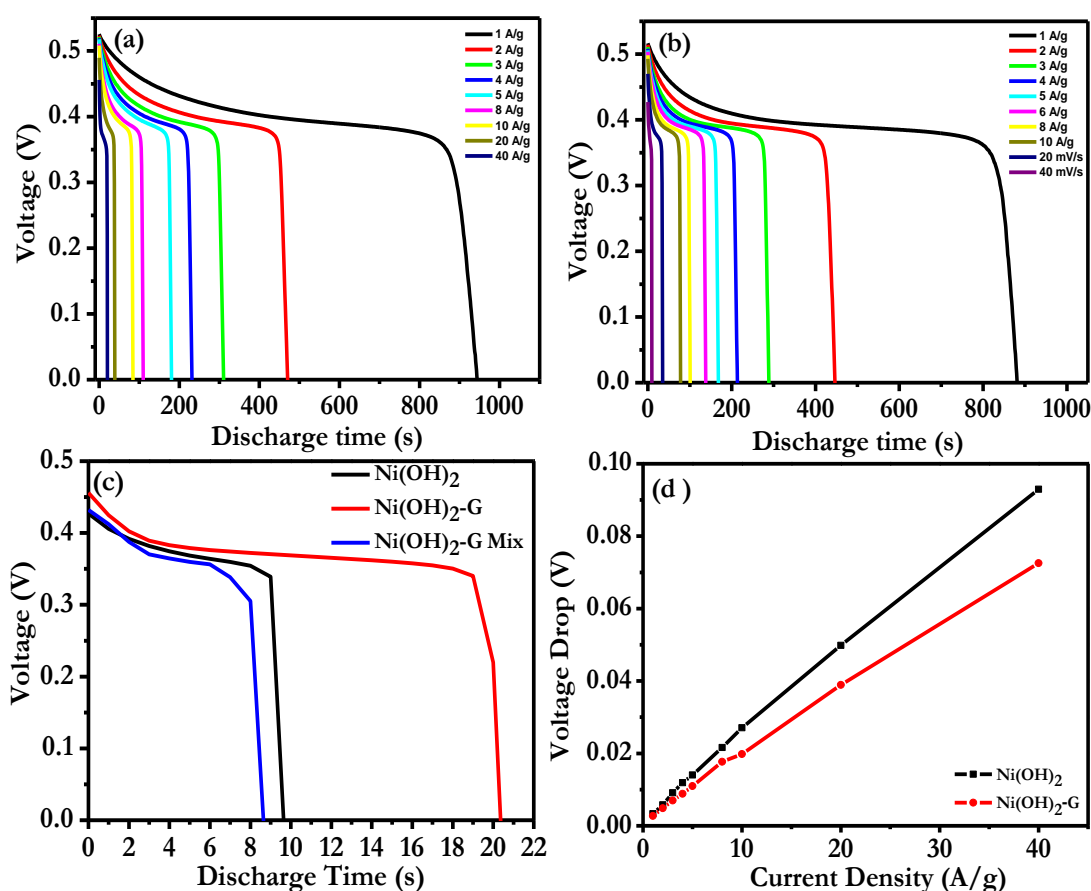
Figure 20. Discharge plots at different current densities for (a) Ni(OH)$_2$-r-GO (from 1 to 40 A/g), (b) Ni(OH)$_2$ (from 1 to 40 A/g), (c) Discharge plot for the Ni(OH)$_2$-r-GO , Ni(OH)$_2$ and physical mixture at a current density of 40 A/g, (d) IR drop against current density for the Ni(OH)$_2$-r-GO and Ni(OH)$_2$

Figure 20c indicates the comparison of the discharge curves at 40 A/g for the Ni(OH)$_2$, Ni(OH)$_2$-r-GO composite and the physical mixture. The composite electrode shows substantially longer (almost double) discharge time over that for bare Ni(OH)$_2$ and mixture, suggesting that Ni(OH)$_2$-r-GO offers more capacitance. Also, it is important to highlight here that the resistive part arising from the voltage drop (IR drop) due to equivalent series

resistance (ESR) of the electrode configuration is more pronounced in the case of bare Ni(OH)$_2$ over its composite (Ni(OH)$_2$-r-GO). Figure 20d shows the plots for IR drop *vs.* current density. It can be seen that Ni(OH)$_2$-r-GO displays much smaller equivalent series resistance (ESR) as compared to bare Ni(OH)$_2$ electrode. This observation was further supported by electrochemical impedance spectroscopy (EIS).

Figure 21a shows the Nyquist plots for the Ni(OH)$_2$ and Ni(OH)$_2$-r-GO samples in the frequency range of 100 mHz to 100 kHz. The real axis intercept which determines equivalent series resistance (ESR) is observed to be higher (1.74 Ω) in the case of Ni(OH)$_2$ as compared to Ni(OH)$_2$-r-GO (0.8 Ω). This can be attributed to the enhanced conductivity in the case of the composite due to r-GO. This further supports the result (please see Figure 20d) of smaller potential drop in the case of Ni(OH)$_2$-r-GO as compared to bare Ni(OH)$_2$.
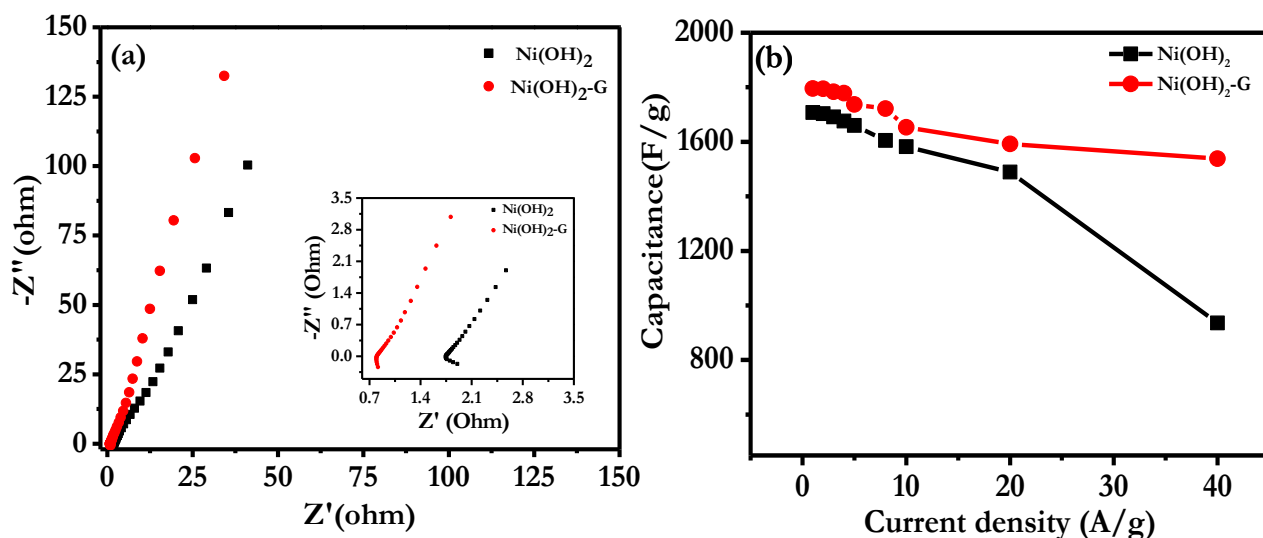
Figure 21. (a) Electrochemical impedance spectra for the Ni(OH)$_2$-r-GO composite and Ni(OH)$_2$. The inset shows the impedance spectra over the higher frequency region.(b) C_s vs. current density plot for the Ni(OH)$_2$-r-GO and Ni(OH)$_2$ from 1 to 40 A/g

Further, a close look at the impedance plot shows a longer Warburg line for Ni(OH)$_2$-r-GO as compared to Ni(OH)$_2$, implying better diffusion of electrolyte ions towards the electrode material in the former case, which is consistent with the BET data. The specific capacitance (C_s) for both electrodes was calculated after 200 cycles.

The *Cs* values at various current densities were calculated from the charge-discharge curves by the equation,

$$Cs = {}^{I \cdot \Delta t}/_{\Delta V}$$

where, C_s is the specific capacitance (F/g), I is the current density (A/g), ΔV is the potential window (V) and Δt is the discharge time (s). *Cs vs.* various current densities were plotted in Figure 10b. The Ni(OH)$_2$-r-GO sample shows a maximum capacitance of 1795 F/g at a current density of 1 A/g whereas bare Ni(OH)$_2$ exhibits a capacitance of 1707 F/g at the same current density. The difference in *Cs* value is thus not that significant at very low current density. At high current density of 40 A/g, however, the Ni(OH)$_2$-r-GO shows a capacitance of 1538 F/g (85.68% retention) whereas bare Ni(OH)$_2$ shows a capacitance of only 936 F/g (only 60.85 % retention). The high capacitance retention even at very high current density is mainly because of the high electrical conductivity of the composite (as confirmed by EIS and galvanostatic charge dischrge profile). Overall this helps in faster charge transfer (decreses in the diffusion length of ions) and also minimizes the ionic diffusion resistance in the bulk of the electrode.

Figure 22 (a, b) shows the CV profiles of Ni(OH)$_2$-r-GO and Ni(OH)$_2$ samples in the 1st, 200th and 1000th cycles at the scan rate of 10 mV/s.
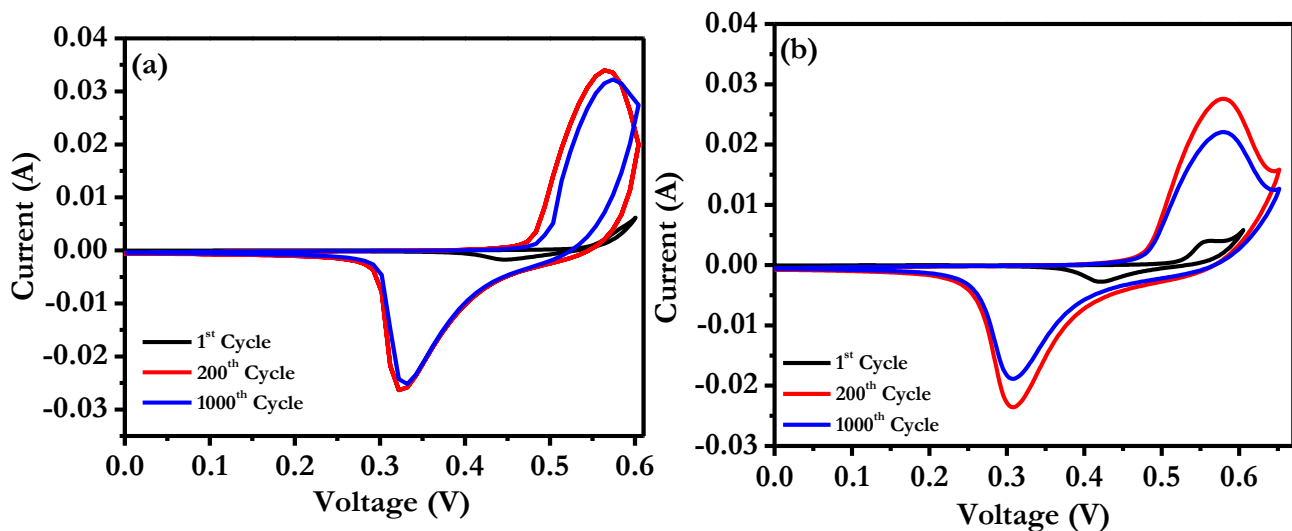

Figure 22. (a) Cyclic stability for the Ni(OH)$_2$-r-GO composite and (b)Ni(OH)$_2$ at the scan rate of 10 mV/s

It is observed that after 200 cycles, there is nominal decrease in current for both of these electrodes which imply good cyclic stability. It is important to mention that the current of both the electrodes is stabilized after 200 cycles.

Figure 23 shows the FE-SEM images for Ni(OH)$_2$-r-GO (a) and Ni(OH)$_2$ (b) electrodes used for electrochemical measurements. It is seen that the average particle size in the case of Ni(OH)$_2$-r-GO is smaller when compared to bare Ni(OH)$_2$. The smaller particle size in the case of composite clearly results in higher density of slit-type pores and increased surface area, leading to enhanced electrochemical performance. This observation also supports our BET data and better performance of the composite when compared to the bare Ni(OH)$_2$.
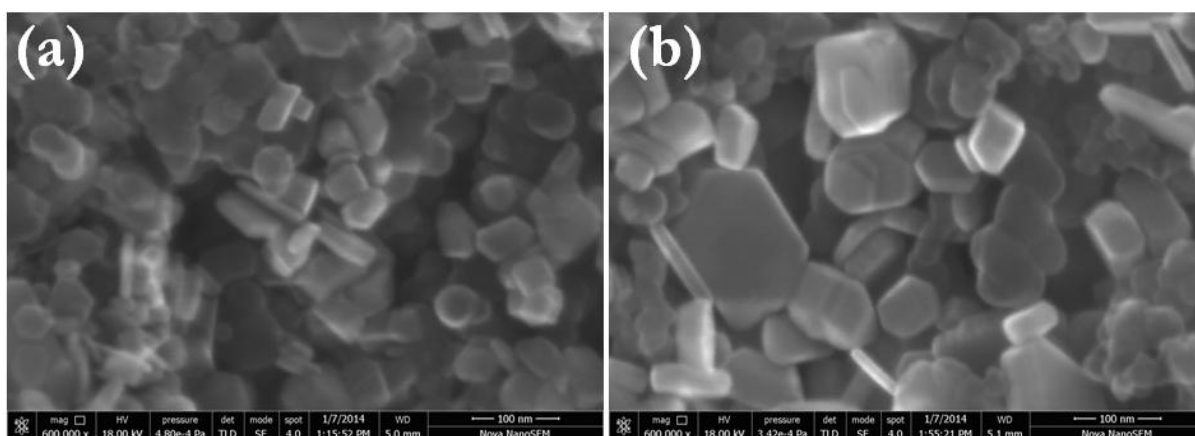
Figure 23. FESEM images of the electrodes of (a) Ni(OH)$_2$-r-GO and (b) Ni(OH)$_2$

The C_s values at low as well as high current densities for Ni(OH)$_2$ and Ni(OH)$_2$-r-GO have been presented in Table 1. This table provides the detailed comparison of recently published reports on C_s values of Ni(OH)$_2$ based electrodes in KOH electrolyte. It can be concluded from the data that the achieved value in our case for Ni(OH)$_2$-r-GO (1538 F/g at 40 A/g) is one of the best values.

We like to point out that most of the other interesting results tabulated for Ni(OH)$_2$ based nanostructured electrodes are synthesized either by using electrodepesition or chemical vapour deposition. Although the results for Ni(OH)$_2$ based electrodes prepared by these techniques are very good, the difficulty associated with them is large scale production and high mass loading. For commercial applications, one needs to manipulate the mass loading and lower cost of manufacturing with satisfactory performance. This important fact motivated us to

develop a simple methodology for bulk scale, surfactant-free synthesis of $Ni(OH)_2$ and its r-GO based composite.

Electrode Structure	Synthesis Method	Electrolyte	C_s at low current density/scan rate	C_s at high current density/ scan rate
$Ni(OH)_2$/ r-GO /Carbon paper (Present work)	**Hydrothermal**	**2M KOH**	**1795 Fg^{-1}@ 1Ag^{-1}**	**1538 Fg^{-1}@ 40 Ag^{-1}**
$Ni(OH)_2$ /Carbon Paper) (Present work)	Hydrothermal	2M KOH	1707 Fg^{-1}@ 1Ag^{-1}	936 Fg^{-1}@ 40 Ag^{-1}
$Ni(OH)_2$/UGF [33]	CVD	6M KOH	1560 Fg^{-1} @ 0.5 Ag^{-1}	1092 Fg^{-1} @ 10 Ag^{-1}
$Ni(OH)_2$/r-GO/NF [34]	Reflux reaction	1M KOH	1828 Fg^{-1} @ 1 Ag^{-1}	780 Fg^{-1} @ 10 Ag^{-1}
$Ni(OH)_2$/Graphene/NF [23]	Co-precipitation	6M KOH	2194 Fg^{-1} @ 2 mVs^{-1}	895 Fg^{-1} @ 20 mVs^{-1}
$Ni(OH)_2$/Graphene/NF [35]	Hydrothermal	6M KOH	1985.1Fg^{-1}@5 Acm^{-2}	912.6Fg^{-1}@ 40 mAcm^{-2}
$Ni(OH)_2$/Graphite/NF [36]	Reflux reaction	6M KOH	1956 Fg^{-1} @ 1Ag^{-1}	1519.9 Fg^{-1} @ 40 Ag^{-1}
$Ni(OH)_2$/Graphene/NF [37]	Precipitation	6M KOH	2134 Fg^{-1} @ 2 mVs^{-1}	822 2 Fg^{-1} @ 70 mVs^{-1}
$Ni(OH)_2$/Graphite [38]	Electrodeposition	5.3M KOH	1850 Fg^{-1} @ 3.2 Ag^{-1}	550 Fg^{-1} @ 11.9 Ag^{-1}
RGO/$Ni(OH)_2$/NF [21a]	Hydrothermal	1M KOH	1667 Fg^{-1} @ 3.3 Ag^{-1}	444.75 Fg^{-1} @ 33 Ag^{-1}
RGO/CNT/$Ni(OH)_2$/ NF [39]	Hydrothermal	2M KOH	1320 Fg^{-1} @ 6 Ag^{-1}	943 Fg^{-1} @ 25 Ag^{-1}
$Ni(OH)_2$/Graphite [21b]	Electrodeposition	1M KOH	1868 Fg^{-1} @ 20 Ag^{-1}	1430 Fg^{-1} @ 40 Ag^{-1}

Table1: Comparison with some recent results.

5. CONCLUSION

In summary, we have demostrated a gram scale, single step, surfactant-free and cost effective synthesis of mesoporous channelled $Ni(OH)_2$ and $Ni(OH)_2$-r-GO composite *via* a simple hydrothermal route. We have employed these materials as electrode materials for supercapacitors (SCs). The charge storage behaviour for both $Ni(OH)_2$ and $Ni(OH)_2$-r-GO was studied in 2M KOH and compared. The $Ni(OH)_2$-G exhibits *Cs* of 1538 F/g at a current density of 40 A/g, whereas only $Ni(OH)_2$ shows the *Cs* of only 936 F/g at the same current density. This excellent performance of composite can be attributed to the increase in the conductivity and surface area due to addition of r-GO.

6. REFRENCES

1. Rolf, E., *Understanding of Material Science.* 2nd Edition ed.; Springer: 2004.

2. Feynman, R., *Engineering and Science Magazine* 1960, p 5.

3. Taniguchi, N. In *Basic Concept of 'Nano-Technology'*, Proceedings of the international conference on production engineering, Tokyo, Tokyo, 1974.

4. Bruchez, M.; Moronne, M.; Gin, P.; Weiss, S.; Alivisatos, A. P., Semiconductor Nanocrystals as Fluorescent Biological Labels. *Science* **1998,** *281* (5385), 2013-2016.

5. Rao, C. N. R., *Chemistry of Nanomaterials.* 2004.

6. Roscher, M. A.; Vetter, J.; Sauer, D. U., Cathode material influence on the power capability and utilizable capacity of next generation lithium-ion batteries. *Journal of Power Sources* **2010,** *195* (12), 3922-3927.

7. Dresselhaus, M. S.; Thomas, I. L., Alternative energy technologies. *Nature* **2001,** *414* (6861), 332-337.

8. Conway, B. E., *Electrochemical Supercapacitors.* Plenum Publishers: USA, 1999.

9. Simon, P.; Gogotsi, Y., Materials for electrochemical capacitors. *Nat Mater* **2008,** *7* (11), 845-854.

10. Winter, M.; Brodd, R. J., What Are Batteries, Fuel Cells, and Supercapacitors? *Chemical Reviews* **2004,** *104* (10), 4245-4270.

11. M. S. Halper, J. C. E., Supercapacitors: A Brief Overview. *The MITRE Corporation, McLean, Virginia, USA.* **2006**, 41.

12. Zhang, L. L.; Zhao, X. S., Carbon-based materials as supercapacitor electrodes. *Chemical Society Reviews* **2009,** *38* (9), 2520-2531.

13. Burke, A., Ultracapacitors: why, how, and where is the technology. *Journal of Power Sources* **2000,** *91* (1), 37-50.

14. Kötz, R.; Carlen, M., Principles and applications of electrochemical capacitors. *Electrochimica Acta* **2000,** *45* (15–16), 2483-2498.

15. (a) Li, H. B.; Yu, M. H.; Wang, F. X.; Liu, P.; Liang, Y.; Xiao, J.; Wang, C. X.; Tong, Y. X.; Yang, G. W., Amorphous nickel hydroxide nanospheres with ultrahigh capacitance and energy density as electrochemical pseudocapacitor materials. *Nat Commun* **2013,** *4*, 1894; (b) Yan, J.; Khoo, E.; Sumboja, A.; Lee, P. S., Facile Coating of Manganese Oxide on Tin Oxide Nanowires with High-Performance Capacitive Behavior. *ACS Nano* **2010,** *4* (7), 4247-4255; (c) Yang, W.; Gao, Z.; Ma,

J.; Wang, J.; Wang, B.; Liu, L., Effects of solvent on the morphology of nanostructured Co3O4 and its application for high-performance supercapacitors. *Electrochimica Acta* **2013,** *112* (0), 378-385; (d) Huang, H.-S.; Chang, K.-H.; Suzuki, N.; Yamauchi, Y.; Hu, C.-C.; Wu, K. C. W., Evaporation-Induced Coating of Hydrous Ruthenium Oxide on Mesoporous Silica Nanoparticles to Develop High-Performance Supercapacitors. *Small* **2013,** *9* (15), 2520-2526.

16. Chang, J.; Sun, J.; Xu, C.; Xu, H.; Gao, L., Template-free approach to synthesize hierarchical porous nickel cobalt oxides for supercapacitors. *Nanoscale* **2012,** *4* (21), 6786-6791.

17. (a) Zhang, Q.; Uchaker, E.; Candelaria, S. L.; Cao, G., Nanomaterials for energy conversion and storage. *Chemical Society Reviews* **2013,** *42* (7), 3127-3171; (b) Gao, M.-R.; Xu, Y.-F.; Jiang, J.; Yu, S.-H., Nanostructured metal chalcogenides: synthesis, modification, and applications in energy conversion and storage devices. *Chemical Society Reviews* **2013,** *42* (7), 2986-3017.

18. Tang, Z.; Tang, C.-h.; Gong, H., A High Energy Density Asymmetric Supercapacitor from Nano-architectured Ni(OH)2/Carbon Nanotube Electrodes. *Advanced Functional Materials* **2012,** *22* (6), 1272-1278.

19. Wang, H.; Liang, Y.; Mirfakhrai, T.; Chen, Z.; Casalongue, H.; Dai, H., Advanced asymmetrical supercapacitors based on graphene hybrid materials. *Nano Res.* **2011,** *4* (8), 729-736.

20. (a) Liu, J.; Sun, J.; Gao, L., A Promising Way To Enhance the Electrochemical Behavior of Flexible Single-Walled Carbon Nanotube/Polyaniline Composite Films. *The Journal of Physical Chemistry C* **2010,** *114* (46), 19614-19620; (b) Gao, Z.; Wang, J.; Li, Z.; Yang, W.; Wang, B.; Hou, M.; He, Y.; Liu, Q.; Mann, T.; Yang, P.; Zhang, M.; Liu, L., Graphene Nanosheet/Ni2+/Al3+ Layered Double-Hydroxide Composite as a Novel Electrode for a Supercapacitor. *Chemistry of Materials* **2011,** *23* (15), 3509-3516.

21. (a) Min, S.; Zhao, C.; Chen, G.; Qian, X., One-pot hydrothermal synthesis of reduced graphene oxide/Ni(OH)2 films on nickel foam for high performance supercapacitors. *Electrochimica Acta* **2014,** *115* (0), 155-164; (b) Lin, Y.; Ruiyi, L.; Zaijun, L.; Junkang, L.; Yinjun, F.; Guangli, W.; Zhiguo, G., Three-dimensional activated reduced graphene oxide nanocup/nickel aluminum layered double hydroxides composite with super high electrochemical and capacitance performances. *Electrochimica Acta* **2013,** *95* (0), 146-154.

22. Yang, G.-W.; Xu, C.-L.; Li, H.-L., Electrodeposited nickel hydroxide on nickel foam with ultrahigh capacitance. *Chemical Communications* **2008,** (48), 6537-6539.

23. Yan, J.; Sun, W.; Wei, T.; Zhang, Q.; Fan, Z.; Wei, F., Fabrication and electrochemical performances of hierarchical porous Ni(OH)2 nanoflakes anchored on graphene sheets. *Journal of Materials Chemistry* **2012,** *22* (23), 11494-11502.

24. Wang, G.; Zhang, L.; Zhang, J., A review of electrode materials for electrochemical supercapacitors. *Chemical Society Reviews* **2012,** *41* (2), 797-828.

25. Hummers, W. S.; Offeman, R. E., Preparation of Graphitic Oxide. *Journal of the American Chemical Society* **1958,** *80* (6), 1339-1339.

26. Fan, X.; Peng, W.; Li, Y.; Li, X.; Wang, S.; Zhang, G.; Zhang, F., Deoxygenation of Exfoliated Graphite Oxide under Alkaline Conditions: A Green Route to Graphene Preparation. *Advanced Materials* **2008,** *20* (23), 4490-4493.

27. D.B. Williams, C. B. C., *Transmission Electron Microscopy – A Textbook for Materials Science*. Springer: 2009.

28. M.D. A. Jorio, R. S., G.F. Dresselhaus, *Raman Spectroscopy in Graphene Related Systems*. Wiley -VHC: 2011.

29. Ferrari, A. C.; Robertson, J., Interpretation of Raman spectra of disordered and amorphous carbon. *Physical Review B* **2000,** *61* (20), 14095-14107.

30. Guo, Y.; Sun, X.; Liu, Y.; Wang, W.; Qiu, H.; Gao, J., One pot preparation of reduced graphene oxide (RGO) or Au (Ag) nanoparticle-RGO hybrids using chitosan as a reducing and stabilizing agent and their use in methanol electrooxidation. *Carbon* **2012,** *50* (7), 2513-2523.

31. Levecque, P.; Poelman, H.; Jacobs, P.; De Vos, D.; Sels, B., Regio- and stereoselective terpene epoxidation using tungstate-exchanged takovites: a study of phase purity, takovite composition and stable catalytic activity. *Physical Chemistry Chemical Physics* **2009,** *11* (16), 2964-2975.

32. (a) Yu, J. G.; Su, Y. R.; Cheng, B., Template-Free Fabrication and Enhanced Photocatalytic Activity of Hierarchical Macro-/Mesoporous Titania. *Advanced Functional Materials* **2007,** *17* (12), 1984-1990; (b) K.S.W Sing, D. H. E., R.A.W. Haul, L. Moscou, R.A. Pierotti, J. Rouqerol, T. Sienieniewska, Reporting physisorption data for gas/solid systems with special reference to the determination of surface area and porosity. *Pure & Applied Chemistry* **1984,** *57* (5), 603-609.

33. Ji, J.; Zhang, L. L.; Ji, H.; Li, Y.; Zhao, X.; Bai, X.; Fan, X.; Zhang, F.; Ruoff, R. S., Nanoporous Ni(OH)2 Thin Film on 3D Ultrathin-Graphite Foam for Asymmetric Supercapacitor. *ACS Nano* **2013,** *7* (7), 6237-6243.

34. Chang, J.; Xu, H.; Sun, J.; Gao, L., High pseudocapacitance material prepared via in situ growth of Ni(OH)2 nanoflakes on reduced graphene oxide. *Journal of Materials Chemistry* **2012,** *22* (22), 11146-11150.

35. Yan, H.; Bai, J.; Wang, J.; Zhang, X.; Wang, B.; Liu, Q.; Liu, L., Graphene homogeneously anchored with Ni(OH)2 nanoparticles as advanced supercapacitor electrodes. *CrystEngComm* **2013,** *15* (46), 10007-10015.

36. Zhang, J. T.; Liu, S.; Pan, G. L.; Li, G. R.; Gao, X. P., A 3D hierarchical porous α-Ni(OH)2/graphite nanosheet composite as an electrode material for supercapacitors. *Journal of Materials Chemistry A* **2014,** *2* (5), 1524-1529.

37. Fang, D.-L.; Chen, Z.-D.; Liu, X.; Wu, Z.-F.; Zheng, C.-H., Homogeneous growth of nano-sized β-Ni(OH)2 on reduced graphene oxide for high-performance supercapacitors. *Electrochimica Acta* **2012,** *81* (0), 321-329.

38. Yin, H.; Wang, D.; Zhu, H.; Xiao, W.; Gan, F., Growing highly capacitive nano-Ni(OH)2 on freshly cut graphite electrode by electrochemically enhanced self-assembly. *Electrochimica Acta* **2013,** *99* (0), 198-203.

39. Chen, X. a.; Chen, X.; Zhang, F.; Yang, Z.; Huang, S., One-pot hydrothermal synthesis of reduced graphene oxide/carbon nanotube/α-Ni(OH)2 composites for high performance electrochemical supercapacitor. *Journal of Power Sources* **2013,** *243* (0), 555-561.